UC Santa Barbara

UC Santa Barbara Previously Published Works

Title

Attenuation and Velocity Tomography of the Northern East African Rift

Permalink

https://escholarship.org/uc/item/4181h4rf

Journal

Journal of Geophysical Research: Solid Earth, 130(2)

ISSN

2169-9313

Author

Eilon, ZC

Publication Date

2025-02-01

DOI

10.1029/2024jb030417

Copyright Information

This work is made available under the terms of a Creative Commons Attribution License, available at https://creativecommons.org/licenses/by/4.0/

Peer reviewed

eScholarship.org Powered by the California Digital Library
University of California

Check for updates

JGR Solid Earth

RESEARCH ARTICLE
10.1029/2024JB030417

Attenuation and Velocity Tomography of the Northern East African Rift

Z. C. Eilon[1]

[1]Department of Earth Science, University of California Santa Barbara, Santa Barbara, CA, USA

Key Points:

- P- and S-wave teleseismic attenuation and travel time are measured within and on the flanks of the Main Ethiopian Rift and Afar
- Congruent 3-D velocity and attenuation tomography depicts upper mantle structure, allowing inversion for temperature, melt, and grain size
- The rift is hot and asymmetric, with strain concentration in west Afar and strain diffusion in the western Ethiopian Plateau

Supporting Information:

Supporting Information may be found in the online version of this article.

Correspondence to:

Z. C. Eilon,
eilon@ucsb.edu

Citation:

Eilon, Z. C. (2025). Attenuation and velocity tomography of the northern East African Rift. *Journal of Geophysical Research: Solid Earth*, *130*, e2024JB030417. https://doi.org/10.1029/2024JB030417

Received 25 SEP 2024
Accepted 1 FEB 2025

Author Contribution:

Conceptualization: Z. C. Eilon
Data curation: Z. C. Eilon
Formal analysis: Z. C. Eilon
Funding acquisition: Z. C. Eilon
Investigation: Z. C. Eilon
Methodology: Z. C. Eilon
Resources: Z. C. Eilon
Software: Z. C. Eilon
Validation: Z. C. Eilon
Visualization: Z. C. Eilon
Writing – original draft: Z. C. Eilon
Writing – review & editing: Z. C. Eilon

© 2025 The Author(s).
This is an open access article under the terms of the Creative Commons Attribution-NonCommercial License, which permits use, distribution and reproduction in any medium, provided the original work is properly cited and is not used for commercial purposes.

Abstract The northern East African Rift, including the Main Ethiopian Rift (MER) and Afar, have been the focus of decades of seismological investigations and dense broadband coverage. Sometimes invoked as an archetype for a narrow continental rift, the confined surficial extension here stands in contrast to geophysical indicators of an asymmetric, broad swath of perturbed mantle. Thermodynamic conditions in this region are challenging to pin down, with melt, temperatures, and perhaps volatiles playing a part in both dynamics and controlling seismic observables. This study presents compressional (P) and shear-wave (S) velocity (V) and attenuation (q) teleseismic tomography of the MER, from rift to flank. This involves a new methodology for measurement and quality control of differential t^* for teleseisms, avoiding extrinsic focusing. This is the most comprehensive body wave travel time and attenuation data set collected in the MER and Afar to date, and the only 3-D attenuation tomography model of a continental rift. Together, the well-resolved co-located models (V_P, V_S, q_S) help constrain the physical conditions within the rift through Bayesian analysis that makes explicit parameter trade-offs. The rift is highly asymmetric, with a sharp eastern boundary but extensive low velocities, high attenuation, and implied melt organization throughout much of the western Ethiopian Plateau, including coincident with volcanism around Lake Tana. A deep-seated plume is connected to shallow rifting. Attenuation and velocity both imply a concentration of extensional strain along the western edge of the Afar triangle.

Plain Language Summary The continent of Africa is splitting apart along the East African Rift. The northern section of this rift, the Main Ethiopian Rift, is narrow and bracketed by steep faults, suggesting the continent splits in a relatively clean break, assisted by upwelling magma. This study presents 3-D models of the breaking tectonic plate and the mantle underneath it. Each model covers an identical area, but looks at the rift in a different way: two models capture different aspects of the speed of seismic wave propagation, and another captures (for the first time, here) how seismic waves lose energy. This latter is often not measured, because it is difficult to calculate. Any one of these models is subject to ambiguities in interpretation of physical parameters we care about (e.g., temperature, where there is magma), but together they offer powerful new insights into the rift. The rift is not everywhere narrow beneath the surface. The western side of the rift has a highly degraded tectonic plate, as deep magma seems to be broadening the rifting from the "bottom up." Meanwhile in the north, effects of rifting appear to be concentrating in the west of the Afar triangle.

1. Introduction

The Main Ethiopian Rift (MER; Figure 1) is an archetype for a "narrow" and strain-focusing continental rift (Buck, 1991; Ebinger & Casey, 2001), as contrasted with "wide" rifts like the Basin and Range. Within the northern MER, currently ~80% of extension is accommodated within a well-defined rift valley that is <30 km wide and circumscribed by clear border faults (Bilham et al., 1999) and includes the majority of Quaternary volcanism and local seismicity (D. Keir et al., 2009). Despite this, there is geodetic (Birhanu et al., 2016; Knappe et al., 2020), geological (Gani et al., 2009), geochemical (Kieffer et al., 2004; Meshesha & Shinjo, 2007; Trestrail et al., 2017), seismic (Asefa & Ayele, 2021) and tomographic (*e.g.*, Chambers et al., 2019) evidence for some distributed extension up to ~400 km beyond the surficial rift boundaries. Plate tectonic models indicate a relatively gradual rift-parallel gradient in divergence rate, mostly well fit by a narrow plate boundary (Stamps et al., 2018, 2021). However, certain aspects of the rift, including the concentration of volcanism and the extent of crustal thinning (Keranen & Klemperer, 2008; Keranen et al., 2009) display heterogeneity along-strike. This likely results from complex, non-linear dynamics and unevenly distributed pre-existing weaknesses. This rift is unusually hot in the global context of continental divergent boundaries (Accardo et al., 2018; Rooney et al., 2012) with particularly low shear wave velocities and strong anisotropy connected to abundant, aligned, upper mantle melt pockets (Hammond et al., 2014; Holtzman & Kendall, 2010; Kendall et al., 2005). The high temperatures,

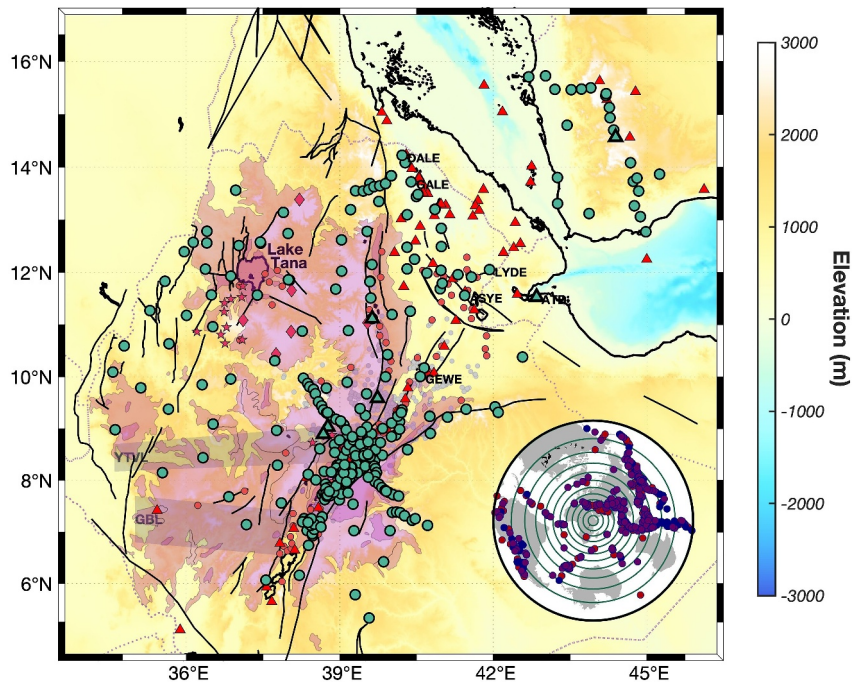


Figure 1. Map of study area, showing locations of seismic stations (green circles), active volcanoes (red triangles), quaternary shield (diamonds) and Strombolian (pentagons) volcanoes, fumaroles and hot springs (red circles), and mapped faults (thin black lines). The outline of the Ethiopian flood basalts is shown in red, while background coloring gives elevation. Thick black lines are coastlines or lake edges, and thin dotted lines are political boundaries. Inset: earthquakes used for this study. Red symbols denote earthquakes for which only P-waves were used, blue denote only S or SKS waves, and purple denote both P and S waves. Green rings give 10° range contours. Named stations are referenced in the text. Bold triangles denote long-lived backbone stations. Shaded polygons show Yerer-Tullu Wellel (YTVL) and Goba-Bonga (GBL) volcanic lineaments.

and potentially ∼11 Ma rift initiation, are linked to >30 Ma mantle plume(s) beneath the region (*e.g.*, Ebinger & Hayward, 1996; Wolfenden et al., 2004) imaged by several recent studies (Boyce et al., 2021; Chang et al., 2020; Civiero et al., 2022; Hansen & Nyblade, 2013; Tsekhmistrenko et al., 2021). Melt has long been recognized as a key component of continental breakup, necessary to overcome plate strength (Bialas et al., 2010; Buck, 2004, 2006). However, the distribution of melt in and adjacent to the rift is not well known, since it is difficult to uniquely attribute seismological observations (chiefly low velocities and anisotropy) to physical mechanisms.

This rift has been comprehensively studied using a variety of seismological tools. Teleseismic earthquake imaging (Bastow et al., 2005, 2008; Benoit, Nyblade, Owens, & Stuart, 2006; Boyce et al., 2021, 2023; Civiero et al., 2015, 2016; Hammond et al., 2013; Hansen & Nyblade, 2013; Van Herwaarden et al., 2023), controlled source seismic (Berckhemer et al., 1975; Mackenzie et al., 2005; Makris & Ginzburg, 1987), ballistic surface wave (Benoit, Nyblade, & Pasyanos, 2006; Chambers et al., 2022), ambient noise (Alemayehu et al., 2023; Chambers et al., 2019; Eshetu et al., 2021; Kim et al., 2012) and combinations thereof (Emry et al., 2019; Petruska & Eilon, 2022) have tomographically probed the MER at a variety of scales. Other geophysical studies have shed light on crustal stress and thinning and upper mantle seismic discontinuities (Ahmed et al., 2022; Cornwell et al., 2010; Dugda et al., 2005; Gauntlett et al., 2024; J. O. S. Hammond et al., 2011; Keranen et al., 2009; Kibret et al., 2022; Lavayssière et al., 2018; Maestrelli et al., 2022; Ogden et al., 2019; Rychert et al., 2012; Stuart et al., 2006; Wang et al., 2021) and the distribution and geometry of shallow melt (Abossie et al., 2023; Bastow et al., 2010; Chambers et al., 2021; Hammond, 2014; Hammond & Kendall, 2016; Kendall et al., 2005). One outcome of these investigations is an apparent dichotomy between the behavior of crust and mantle lithosphere: ultralow upper mantle velocities appear to require thinned or absent mantle lithosphere in the rift, in contrast to limited crustal stretching factors (Holtzman & Kendall, 2010; Lavayssière et al., 2018; Maguire et al., 2006). This conundrum, observed or invoked elsewhere (Driscoll & Karner, 1998; Eilon et al., 2016; Kington & Goodliffe, 2008; Lavier & Manatschal, 2006; Manatschal, 2004), requires mechanisms to thicken crust (*e.g.*, magmatic

21699356, 2025, 2, Downloaded from https://agupubs.onlinelibrary.wiley.com/doi/10.1029/2024JB030417 by University Of California Santa Barbara, Wiley Online Library on [14/02/2025]. See the Terms and Conditions (https://onlinelibrary.wiley.com/terms-and-conditions) on Wiley Online Library for rules of use; OA articles are governed by the applicable Creative Commons License

21699356, 2025, 2, Downloaded from https://agupubs.onlinelibrary.wiley.com/doi/10.1029/2024JB030417 by University Of California Santa Barbara, Wiley Online Library on [14/02/2025]. See the Terms and Conditions (https://onlinelibrary.wiley.com/terms-and-conditions) on Wiley Online Library for rules of use; OA articles are governed by the applicable Creative Commons License

underplating, lower crustal flow) or preferentially thin lithospheric mantle. The importance of melt and/or small-scale convection as agents for non-mechanical lithospheric removal has been theorized (Havlin et al., 2013) but not demonstrated.

Despite this surfeit of imaging, high-resolution observations of seismic attenuation have never been brought to bear on this rift. Moreover, data that extend broadband coverage well beyond the rift axis call for upper mantle models of the MER and flank with parallel treatment of shear and compressional structure. This study presents the first systematic measurement of teleseismic body wave attenuation within, and adjacent to, the MER. The East African rift is a natural laboratory that combines excellent and broad instrumental coverage with high temperatures close to the surface that should activate anelastic grain-scale deformation mechanisms that cause attenuation. Attenuation provides a powerful complement to more conventional observations of seismic velocity, due to its distinct sensitivity to melt, grainsize, and temperature near the solidus and relative insensitivity to composition (*e.g.*, Dalton et al., 2009). Allying these two parameters, therefore, offers new opportunities to interpret mantle structure and understand physical mechanisms underlying observed heterogeneity. The goals of this study are: To make new, high quality measurements and tomographic models of seismic velocity and attenuation in this rift; To compare these parameters against each other and against prior observations; To shed new light on physical properties of the northern East African Rift and rifting processes.

2. Data

I use broadband seismic data from 14 seismic networks deployed between 1999 and 2017 in the region of the northern East African rift roughly between 5 to 16° N and 34 to 45° E (Figure 1). These data were collected by a variety of groups, with DOI's and PIs listed in the *Data Availability* and *Acknowledgments* sections. Most arrays in this data set were temporary, with <2 years durations. Some long-lived "backbone" stations in the data set have been recording for as long as 18 years; these stations tie differential measurements from non-coeval deployments together. I use three-component broadband instruments, with channel codes HH* or BH*.

I obtained a catalog of earthquakes from FDSN at all depths with moment magnitudes between 6.0–7.9 (Figure 1). The permitted station-event distance ranges were as follows: *P*-waves: 30–100°, *S*-waves: 30–84°, *PP*-waves: 63–140°, *SKS*-waves: 86–132, *PKS*-waves: 129–140°. Waveforms were downloaded from the IRIS DMC and corrected for previously published component mis-orientations, instrument response (to velocity), filtered with a 0.01 Hz high-pass, and down-sampled to 10 Hz using a low-pass Nyquist anti-aliasing filter.

3. Methods

3.1. Body Wave Differential Travel Time and Differential Attenuation Measurements

I measured differential travel time (ΔT, stage 1) and differential attenuation (Δt^*, stage 2) on teleseismic *P*, *PP*, *S*, *SKS*, and *PKS* waveforms (Figure 2). XKS phases complement the direct-S phases by contributing unique raypath geometries. Both stages involved quality control (QC) steps described below and in Text S1 in Supporting Information S1, and good ΔT measurements were required to attempt Δt^* measurements on the same seismogram. Earthquakes with <4 measurements were not used.

Stage 1: I measured differential travel times using multichannel cross-correlation (VanDecar & Crosson, 1990), relative to IASP91 move-out (Kennet & Engdahl, 1991). Data were visually inspected, and nominal two-pole Butterworth filters of [1–0.2 Hz] for *P*-waves and [1–0.083 Hz] for *S*-waves were adjusted for each earthquake to minimize noise while preserving the highest possible frequency content. Time windows were manually adjusted to include at least 10 s of pre-arrival baseline and as little of the seismogram following the first phase oscillation as possible, avoiding near-surface reverberations. Noisy or anomalous traces were manually removed. An automated measurement algorithm involved iterative cross correlation, waveform alignment and stacking, and rejection of individual waveforms based on a threshold cross-correlation coefficient (CCC) of 0.75 with the stack. This process was repeated until all CCC values met this criterion or <4 waveforms remained.

Stage 2: I measured differential attenuation through joint fitting of amplitude and phase spectra (Figure 2, Figure S1 in Supporting Information S1). Frequency-dependent phase lags (predicted from physical dispersion) augment amplitude information (*e.g.*, Eilon & Abers, 2017). Quality controls for this step are described in the supplement (Text S1 in Supporting Information S1). Inter-station differential attenuation

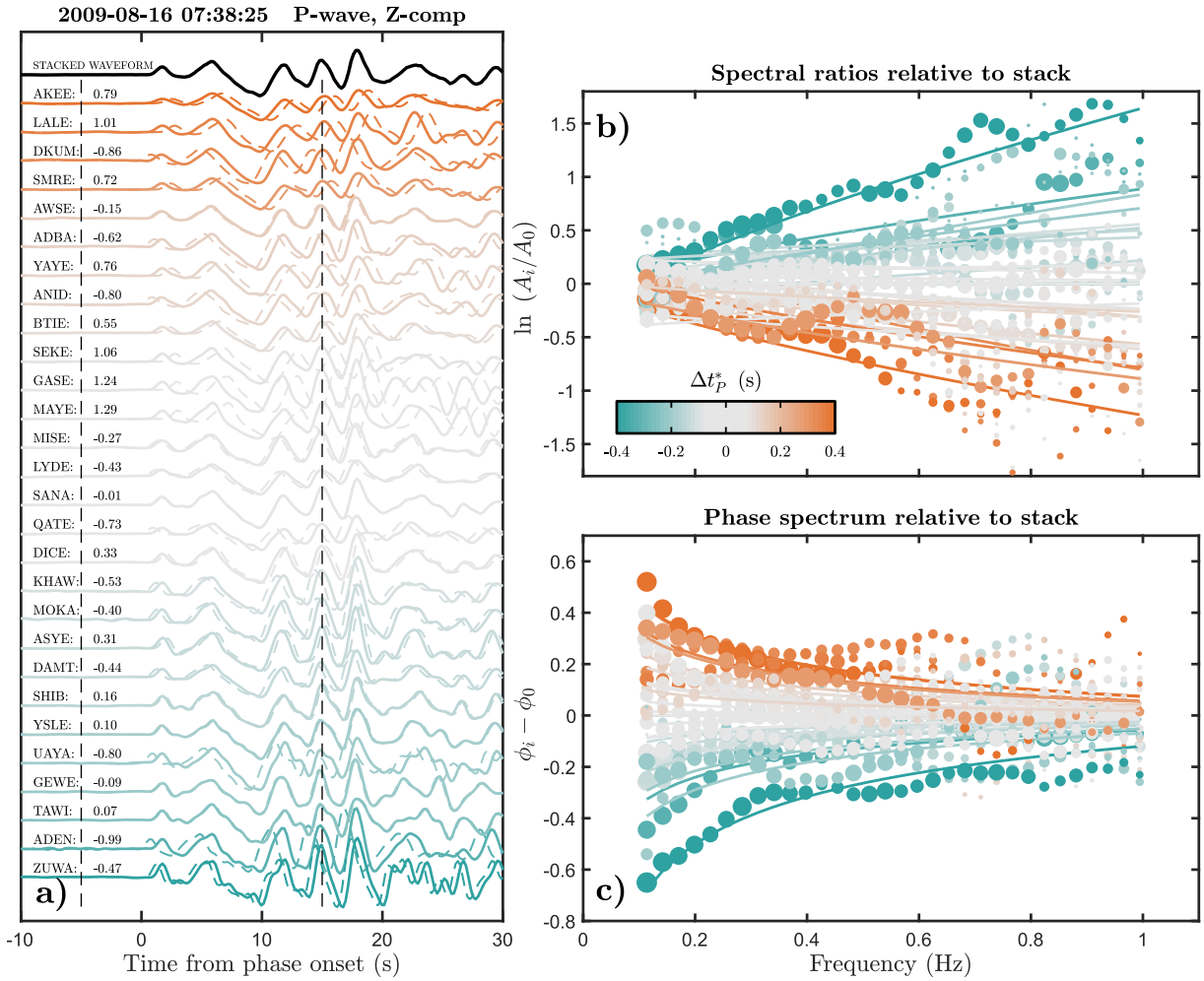


Figure 2. Differential travel time and attenuation measurement. (a) Record section of P-wave on the vertical component, filtered 1–50 s, recorded at a subset of stations in the total data set. Solid lines: post-time-shifted data, dashed lines are moveout-adjusted original. Narrow black lines: time window for attenuation measurement. Black text: station names and measured dT values (positive means late/slow). (b) Measured (circles) and best-fit (line) log differential amplitude spectra. Circle diameters are proportional to the weighting of the measurement at that frequency. (c) As for (b) but differential phase spectra. Both (b) and (c) show differential values relative to the event stack (black line in panel (a)) for illustration purposes; the actual measurements are made pairwise for all two-station combinations and a unique Δt^* value is then obtained for each individual station by least squares. Data are colored by best fit Δt^* value.

(Δt^*) was measured pairwise by simultaneous fitting of relative amplitude and phase spectra ($A(f)$ and $\phi(f)$, respectively; Figure 2) from 0.025 to 1 Hz in a manner similar to Eilon and Abers (2017). Here, I modify that method (Figure S1 in Supporting Information S1) to compute complex spectra (using the same signal window as above) using standard Fourier decomposition, rather than using a comb of narrow-band filters. This modification reduces error in the measurements of differential phase, and produces phase and amplitude spectra that are more self-consistent. I assumed frequency dependence $Q = Q_0 f^{\alpha}$ (with $\alpha = 0.27$ as determined from experiments (Abers et al., 2014; Jackson et al., 2002)), and report Δt^* corrected to 1 Hz, according to

$$\ln\left(\frac{\mathrm{A_i(f)}}{A_j(f)}\right) = \ln\left(\frac{A_i^0}{A_j^0}\right) - \pi f_0^{\alpha} f^{1-\alpha} \Delta {t_{ij}}^*$$

$$\phi_i(f) - \phi_j(f) = \psi + \frac{1}{2}\cot\left(\frac{\alpha\pi}{2}\right)\left(\frac{f}{f_0}\right)^{\alpha} \Delta t_{ij}^*$$

21699356, 2025, 2, Downloaded from https://agupubs.onlinelibrary.wiley.com/doi/10.1029/2024JB030417 by University Of California Santa Barbara, Wiley Online Library on [14/02/2025]. See the Terms and Conditions (https://onlinelibrary.wiley.com/terms-and-conditions) on Wiley Online Library for rules of use; OA articles are governed by the applicable Creative Commons License

21699356, 2025, 2, Downloaded from https://agupubs.onlinelibrary.wiley.com/doi/10.1029/2024JB030417 by University Of California Santa Barbara, Wiley Online Library on [14/02/2025]. See the Terms and Conditions (https://onlinelibrary.wiley.com/terms-and-conditions) on Wiley Online Library for rules of use; OA articles are governed by the applicable Creative Commons License

Where A^0 is a frequency-independent gain factor at each station, f_0 is the reference frequency (1 Hz), and ψ is a frequency-independent (or "infinite frequency") phase difference due to heterogeneous anharmonic velocities. The amplitude spectral fit is upweighted by a factor of γ relative to the phase spectra for the Δt^*_{ij} estimates, where $\gamma = 2$. i and j are station indices; pairwise measurements (for all $i \neq j$) are then inverted for single station differential values Δt_k ($k \in 1 : N^{\text{sta}}$) using a weighted least-squares approach, with the constraint that $\sum \Delta t^*_k = 0$.

Body wave attenuation measurements are noisy (*e.g.*, Bezada et al., 2019). Errors arise from the presence of stochastic noise, from the finite signal width used to estimate spectra, from extraneous phases (crustal reverberations, etc.) within the time window, and from extrinsic dispersive effects (elastic scattering and focusing) altering the spectra. This latter effect is of particular concern at plate boundaries with large gradients in seismic velocity, such as rifts.

Stochasticity is addressed through quality controls (Text S1 in Supporting Information S1) and maximizing the number of good quality measurements so that subtle signals overcome noise. To mitigate against spectral noise, I weighted each frequency in the spectral fitting by the similarity in amplitude calculated by Fourier decomposition versus the multitaper method (Thomson, 1982). For the final station Δt^*_k inversion, each pairwise attenuation measurement was weighted by a posteriori spectral fitting error. Finally, to address extrinsic effects, I exploit the fact that scattering and focusing cause phase and amplitude spectral slopes to diverge (Allen et al., 1999; Pang et al., 2023; Soto Castaneda et al., 2021) or otherwise not co-vary in a manner consistent with the prediction for intrinsic attenuation. I created a metric to identify this disagreement by varying the γ factor between extremes (for this test only, not for the actual measurements), and measuring changes in apparent Δt^*_{ij}, apparent $\ln\left(\frac{A^0_i}{A^0_j}\right)$, apparent ψ, and the weighted goodness of fit to both sets of spectra. In the ideal case with no noise and only intrinsic attenuation, all values are unchanged as γ is varied: the metric would be zero. In the presence of noise, the metric is non-zero, but still small (<5). As extrinsic effects become more significant, this metric increases (Figure S2 in Supporting Information S1). Based on a series of synthetic tests, I used a cautious empirical cut-off of 3 for this metric; waveforms with a higher score than this are eliminated. For reference, the best-behaved spectra yield values on the order of 0.05, obviously spurious spectra produced values >90. This QC step is performed iteratively, twice.

3.2. Attenuation and Velocity Tomography

Differential attenuation and travel time measurements were inverted tomographically on the same grid for three-dimensional models of differential attenuation and velocity. The resultant models allow direct comparison of these parameters within a continental rift for the first time.

The velocity model is parameterized as fractional slowness perturbations ($\delta s = \Delta s / s_0$) from the 1-D IASP91 reference slowness ($s_0 = 1/V_0$) (Kennet & Engdahl, 1991). Throughout this paper, "δ" denotes a fractional change, "Δ" a differential value, and subscript "0" a reference value. The attenuation model is similarly parameterized in terms of fractional attenuation perturbations ($\delta q = \Delta q / q_0$), where q is the inverse of the quality factor: $1/Q$. The starting model for the attenuation inversion is discussed in more detail below. Both models are defined on the same irregular, rectangular grid of nodes with horizontal spacing of 30–60 km (densest in the area spanned by stations, sparsest 750 km beyond the edge stations) and vertical spacing of ∼30 km at the surface stretching to 60 km at the base of the models: 710 km depth.

In both cases, I solved for mantle structure using a damped, weighted linearized inversion. Rays were traced in 1-D in IASP91. For velocities, I used a first Fresnel zone paraxial approximation to the Born theoretical finite frequency sensitivity kernel (Eilon et al., 2015; Schmandt & Humphreys, 2010), with updated normalization and voxel-volume terms (Brunsvik et al., 2021), using the center frequency of the travel-time measurement filter. Similar kernels are not well defined for differential attenuation measurements (which are corrected to 1 Hz but are definitionally sensitive to Earth's anelastic response across the measurement frequency range). Absent a thorough treatment of teleseismic attenuation kernels, beyond the scope of this study, I implement a simple "ray-in-box" approach to constructing the $\partial \Delta t^* / \partial \delta q$ kernels by linearly interpolating Δt^* gradient values for 5 km segments along the ray to the eight nodes at vertices of the grid cell that contains that segment. For ray i and model parameter m_j, the element of the linearized data kernel (G) for the differential attenuation measurement, is thus:

$$G_{ij} = \frac{\partial \Delta t_i^*}{\partial m_j} = \frac{\sum_k (x_{ijk} r_{ik})}{V_j^0 Q_j^0}$$

Where the superscript "0" refers to starting model values, r_{ik} are all k segment lengths along the ith ray, and x_{ijk} are the cuboidal interpolation weights of that ray segment at the jth node.

I account for the large crustal variations throughout the area by first computing differential travel times predicted from crustal thickness and velocity variations alone as inferred from a smoothed Moho (and Vp/Vs ratio) model that combines constraints from several active source and receiver function studies (Ahmed et al., 2022; Dugda et al., 2005; Hammond et al., 2011; Keranen et al., 2009; Kibret et al., 2022, 2023; Maguire et al., 2006; Ogden et al., 2019; Stuart et al., 2006; Wang et al., 2021). These differential times, which account for individual arrivals' ray parameters, are subtracted from the data before inversion; station static terms in the inversion allow for further effective perturbations to shallow structure to reduce misfit (Figure S22 in Supporting Information S1). This crustal correction was only made for travel times, not Δt^*.

For teleseismic body wave velocity tomography, we rarely worry about the "starting model" of absolute slownesses which dictates sensitivity of travel times to perturbational slowness. This is because the difference in travel-time sensitivity between two initial models that differ by ΔV is $\Delta V / V_{\text{avg}}$. Since coarse velocity structure is generally known to within <<10%, the effect of uncertainty in these absolute values makes only second order difference to the final model of fractional slowness perturbation. However, in the case of attenuation tomography, this is not the case; proposed models of absolute Q can vary by orders of magnitude in a given location. This has profound effects on the model sensitivity to Δt^*, and hence the tomographic differential attenuation model (Figure S6 in Supporting Information S1). Q is thought to be highly stratified at large (*e.g.*, Dziewonski & Anderson, 1981) and small (*e.g.*, Russell & Dalton, 2022) scales, with a thin, low-Q "asthenosphere" layer far more attenuating than the lithosphere or deeper mantle (Durek & Ekström, 1996; Lawrence & Wysession, 2006). Δt^* will have greatest sensitivity to δq ($= \Delta q / q$) in the asthenosphere. For inversions with constant damping, this high sensitivity will "squeeze" δq structure into this layer (Figure S6 in Supporting Information S1), whether or not the data really prefer structure to concentrate here. In this study, I use a starting Q_S from the QsADR17 model (Adenis et al., 2017; Debayle et al., 2020). I calculate Q_P from this model by assuming a bulk quality factor $Q_\kappa = 943$ (Durek & Ekström, 1996), cognisant that this effectively rules out attenuation in bulk (Section 5.3).

3.3. Regularization

To stabilize the inversion, I implemented both model norm damping and first-derivative flattening (*i.e.*, minimizing the norm of the first derivative vector in each dimension). Each is controlled by a separate, tuneable parameter. I used L-tests (Figure S4 in Supporting Information S1) to determine optimal regularization parameters separately for velocity and attenuation models, and S and P models, due to differing data coverage and data error. L-tests illuminate fit-versus-norm trade-offs, but traditional L-tests still require defining the balance of higher fit and lower model complexity. This can be improved by exploiting "training" and "validation" data sets in L-tests (Ma et al., 2024). For each combination of trial regularization parameters, I first performed the inversion on a "training" data set (a randomly chosen 80% of the data). The resultant model was then used to predict the full data set, including the 20% "validation" data. At high regularization, data fit is poor overall. At intermediate regularization, the fit to both training and validation sets is good, since both sample the same seismic structure, which the model now hopefully approximates. At low regularization, the training data set is over-fit, but the fit to the validation data will deteriorate from its optimum. I repeated these L-tests over four iterations, each time sampling a new validation data set, and taking an average over the four. The validation sampling was quasi-random; validation data were drawn roughly evenly across stations and back-azimuths, to avoid training and validation data sets having wholly different regions of coverage. This approach offers significant promise for identifying optimal regularization, but is not a panacea. Minima in validation data set fit are broad enough that some user-defined choices are still required.

I separately penalized model norm and model roughness, searching over regularization parameters to minimize the penalty function

$$X = a\left\{\|\mathbf{m}\|_2 + \|\nabla \mathbf{m}\|_2\right\} - b\left\{\mathrm{VR}^{\mathrm{ALL}}(\mathbf{m})\right\} - c\left\{\mathrm{VR}^{\mathrm{VAL}}(\mathbf{m})\right\}$$

21699356, 2025, 2, Downloaded from https://agupubs.onlinelibrary.wiley.com/doi/10.1029/2024JB030417 by University Of California Santa Barbara, Wiley Online Library on [14/02/2025]. See the Terms and Conditions (https://onlinelibrary.wiley.com/terms-and-conditions) on Wiley Online Library for rules of use; OA articles are governed by the applicable Creative Commons License

21699356, 2025, 2, Downloaded from https://agupubs.onlinelibrary.wiley.com/doi/10.1029/2024JB030417 by University Of California Santa Barbara, Wiley Online Library on [14/02/2025]. See the Terms and Conditions (https://onlinelibrary.wiley.com/terms-and-conditions) on Wiley Online Library for rules of use; OA articles are governed by the applicable Creative Commons License

Where VR(**m**) is the weighted variance reduction (a measure of fit) for the entire data set, "ALL" and "VAL," refer to the full data set and the training data set, and ∇ denotes the 3-D first derivative operator. a, b, and c are user-defined constants (of which only two are truly independent). { } operators denote normalization in the range 0–1 between the maximum and minimum values found in the grid search. I select values of a, b, and c to be 5, 1, and 2 respectively for velocity inversions, and 6, 4, and 1 for attenuation inversions.

3.4. Testing the Model

To understand model robustness, I conducted two types of synthetic test: (a) Recovery tests, where synthetic structure is used to forward-calculate synthetic data that is then inverted to determine how the inversion process filters certain features, if they existed. These include checkerboard (Figures S7–S14 in Supporting Information S1) and spike (Figures S31–S42 in Supporting Information S1) tests. (b) Squeezing tests, using strong norm damping to prevent structure entering the model beneath a certain "squeezing" depth (Figures S23–S28 in Supporting Information S1). These tests ascertain the extent to which the data *require* structure beneath a squeezing depth (if deep structure is not required, then squeezed models will fit the data just as well as models where more vertical smearing is permitted).

4. Results

4.1. Teleseismic Measurements

The total data set comprises 22,074 ΔT values (10970 *P*, 2583 *PP*, 4107 *S*, 4067 *SKS*, and 347 *PKS*) and 10,106 Δt^* values (6656 *P*, 1256 *PP*, 1876 *S*, 1452 *SKS*, and *91* PKS), obtained from 941 unique earthquakes with arrivals in the distance range 30°–137°, recorded on 340 unique stations. *P*-wave measurements had a maximum azimuthal gap of ∼17°, centered at 124°. *S*-wave measurements had a maximum azimuthal gap of ∼30°, centered at 165° (Figure 1).

4.1.1. Travel Time Data

ΔT data for P and S waves show similar patterns (Figure 3). The range in arrival times (using 95% bounds) is +0.97 s (*i.e.*, delayed) to −1.02 s for *P*-waves (RMS = 0.52 s), and +2.33 s to −3.34 s for *S*-waves (RMS = 1.37 s). The clearest spatial pattern, conforming to previous observations (*e.g.*, Bastow et al., 2008; Boyce et al., 2021; Kounoudis et al., 2021), is slow arrivals along the axis of the MER, bracketed by faster arrivals. West of the axis, slow arrivals extend >300 km beyond the main surficial expression of the rift valley. By contrast, the eastern flank has an abrupt transition to very fast relative arrivals ∼50 km from the border faults.

In the Afar, travel time delays are also asymmetric. A swath of slow arrivals follows the western boundary of the depression, while arrivals in northwest Afar are fast. Uniformly fast arrivals at some Afar stations (*e.g.*, DALE, GALE) indicates thinner-than-average crust. Crustal thickness varies by as much as a factor of two (40 km to <20 km) over short distances in Afar (Hammond et al., 2011; Makris & Ginzburg, 1987), with particularly steep Moho relief at the Depression's western edge (Ahmed et al., 2022) and maximal crustal thinning in the western portion of the Depression (*e.g.*, Kibret et al., 2023). Indeed, accounting for crustal thickness variations (Figure S3 in Supporting Information S1) actually accentuates the apparent abruptness of the travel time gradients between the rift and its flanks. That said, even accounting for crustal effects, it appears that the mantle just west of the Afar triangle is slower than central Afar, which itself is slower than northern or south-eastern Afar. Central-to-western Afar is one of very few areas of mild dissimilarity between the ΔT_P and ΔT_S data sets. Here, slow ΔT_P values are concentrated west of the topographic depression, while slow ΔT_S is more evenly distributed and extends further to the north east.

I find a statistically robust ($R^2 = 0.61$) correlation between *P* and *S*-wave travel times measured between common earthquake-station pairs, which clearly covary ($\sigma_{12} = 0.54$) (Figure 4). $\Delta T_S/\Delta T_P$ slope estimated using the gradient of the first component from principal component analysis (PCA; which accounts for error in both data sets) is 3.79 for the entire data set, implying high average d ln V_S/d ln V_P of 2.09, assuming $V_P/V_S = 1.81$. Station-averaged delay times show a similar trend (Figure 4) with even higher correlation coefficient ($R^2 = 0.70$) but lower apparent d ln V_S/d ln V_P of 1.69. Restricting this analysis to just measurements at stations within the region of the MER yields an even greater d ln V_S/d ln V_P of ∼2.19, while the off-rift Ethiopian highlands have a lower d ln V_S/d ln V_P value of ∼1.82. Previous studies here using similar ΔT_P-versus-ΔT_S regressions have

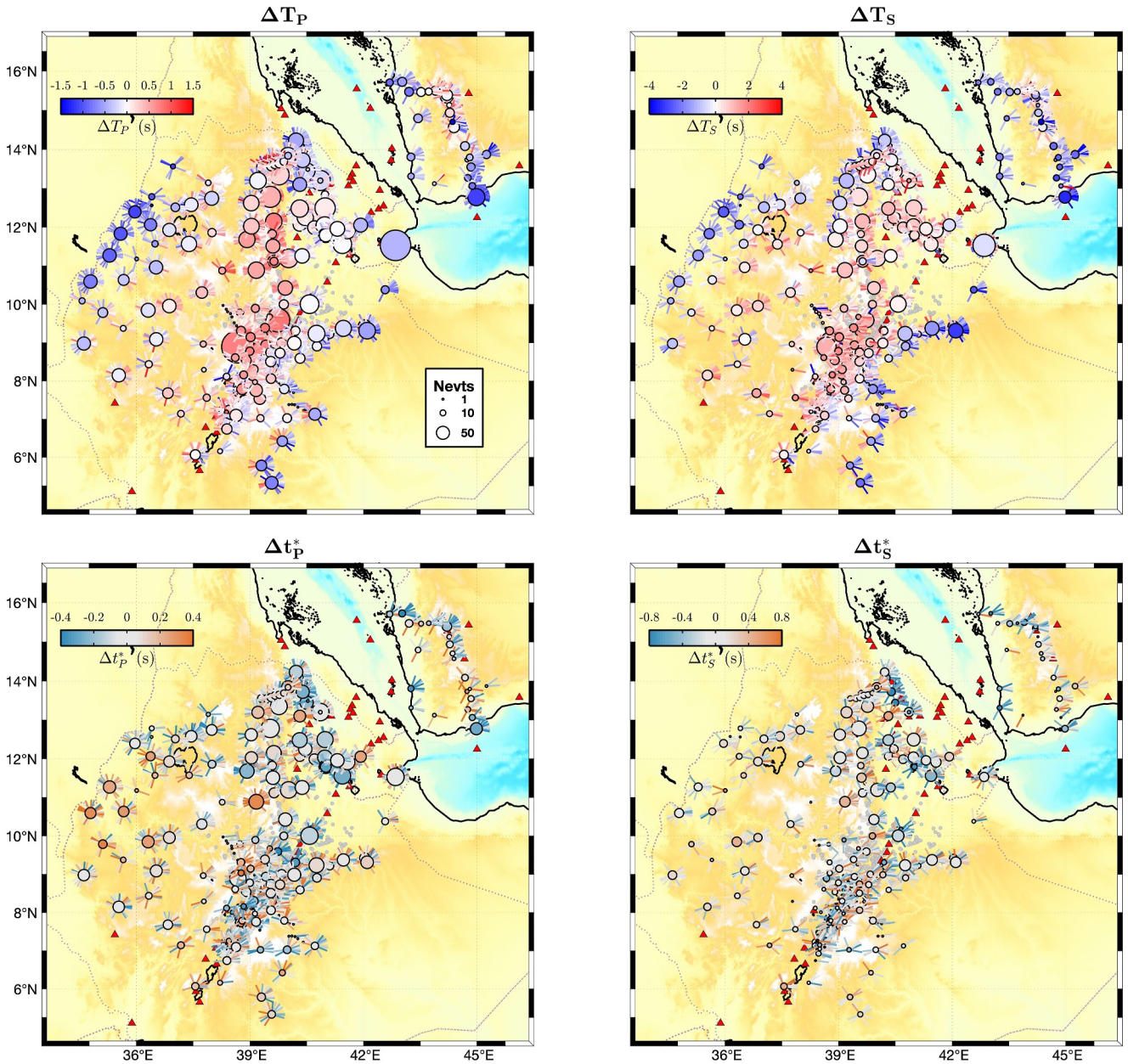


Figure 3. Maps showing all differential travel time measurements (ΔT; upper) and differential attenuation (Δt^*; lower) for P (left) and S, SKS, and PKS collated (right). Measurements are depicted as spokes protruding from station locations in the direction of the station-event azimuth, colored by measured value. Circles give the station-average values (solved for using a least squares approach, accounting for event terms), with size proportional to the number of measurements. Red triangles are volcanoes, heavy black lines are coastlines or lakes, and light dotted lines are political boundaries.

found similar or higher values of apparent $\mathrm{d}\ln V_S/\mathrm{d}\ln V_P$: correcting to the same V_P/V_S ratio, Bastow et al. (2005) estimated ~2.76 across the MER (and far higher within the rift) and Civiero et al. (2016) saw 2.04 (with 3.1 inside the rift).

4.1.2. Differential Attenuation Data

The Δt^* data are messier (Figures 3 and 4) and evince noisiness typical of this measurement (*e.g.*, Cafferky & Schmandt, 2015; Hwang et al., 2011; Soto Castaneda et al., 2021). Inherent noise is compounded by relatively modest signal amplitude predicted for all but the most attenuating regions; rays accrue Δt^* much more gradually

21699356, 2025, 2, Downloaded from https://agupubs.onlinelibrary.wiley.com/doi/10.1029/2024JB030417 by University Of California Santa Barbara, Wiley Online Library on [14/02/2025]. See the Terms and Conditions (https://onlinelibrary.wiley.com/terms-and-conditions) on Wiley Online Library for rules of use; OA articles are governed by the applicable Creative Commons License

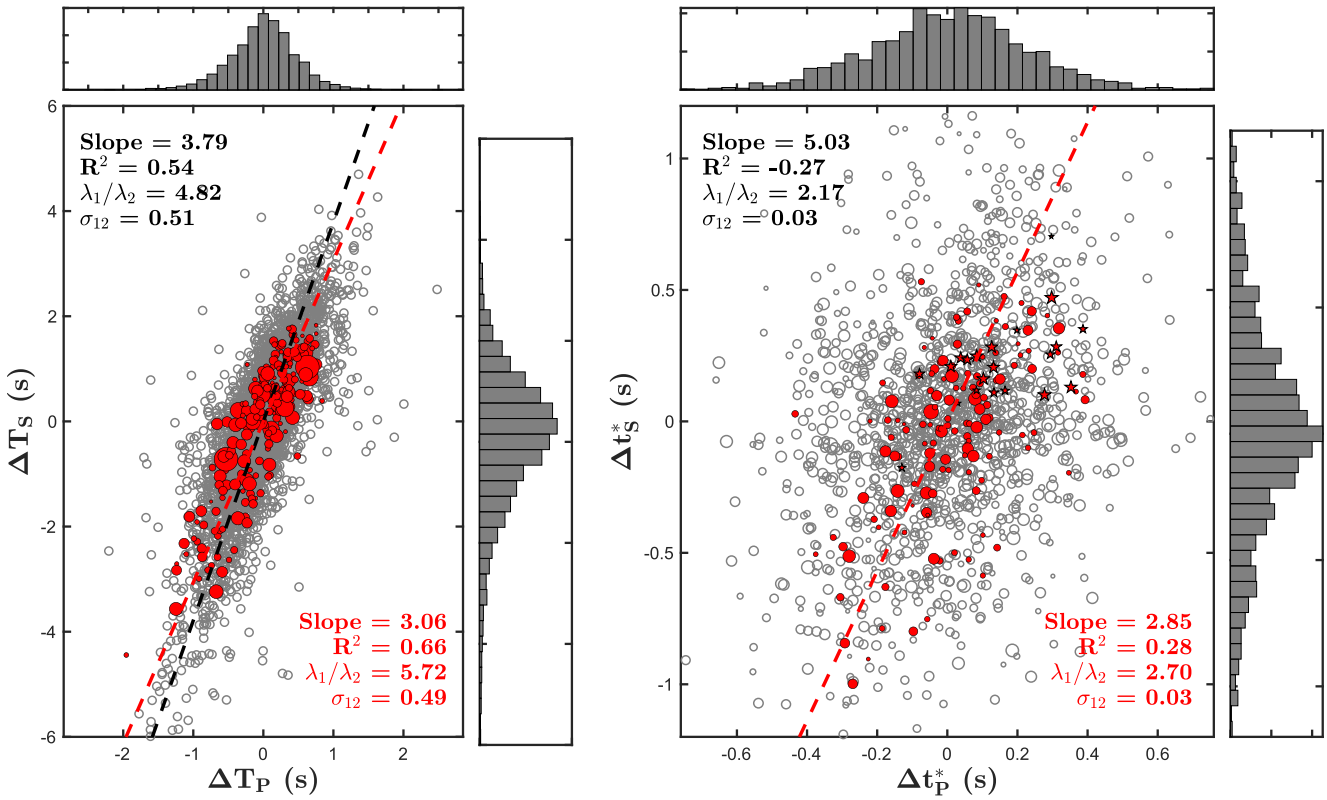


Figure 4. Comparison of P- and S-wave ΔT (left) and Δt^* (right) measurements (subsets of the full data set, since for some earthquake-station pairs either P or S was not measured) relative to the mean. Gray denotes individual measurements and red denotes station averages (Figure 3). Stations on the Ethiopian plateau are given star symbols for the Δt^* plot. Symbol size is inversely proportional to estimated standard deviation. Histograms show marginal distributions of individual measurements. Dashed lines are best fitting linear relationships from principal component analysis, where significant. Inset values are gradient, R^2, the ratio of the maximum/minimum eigenvalues (λ_1/λ_2), and the covariance (σ_{12}) of the data.

than they accrue ΔT. Using 95% bounds, P-wave Δt^* varies from +0.49 s to −0.48 s (positive means more attenuated) while for S-waves this range is +0.96 s to −0.96 s. The Δt^* RMS values are 0.24 s for *P*-waves and 0.47 s for *S*-waves. The most consistently positive (more attenuating) Δt^* values are recorded in the western portion of Afar, and the most consistently negative Δt^* values are seen in northern Afar, Yemen, and on the south east flank of the MER.

A striking aspect of the Δt^* measurements is that they do not straightforwardly mirror the travel time observations. Some stations recording ubiquitously delayed arrivals do not record obviously high (more attenuating) Δt^*. For instance, central Afar stations show mostly negative differential attenuation in *P* and mixed attenuation in *S*. By contrast, western Afar stations (which see slow arrivals) *do* more consistently record high attenuation. Measurements close to the MER axis are inconsistent, with substantial changes in apparent Δt^* over short distances, but modestly more positive attenuation outside of, and particularly just east of, the northern rift valley. No statistically robust correlation can be drawn between ΔT and Δt^* values for either *P* or *S*-waves when averaging over the whole study region, or in most sub-regions. One small exception to this rule is the Ethiopian Plateau, where a *negative* correlation is observed between station-averaged *P*-wave attenuation and travel time ($R = -0.57$).

All that said, the attenuation measurements are clearly not random; individual stations record mostly consistent low or high Δt^*, and spatial patterns are easy to pick out by eye. Several stations manifest clear and systematic back-azimuthal variation, for instance west of the Afar depression at ~39°E where more attenuation is measured for arrivals from the east. Most stations record similarly positive or negative *P*- and *S*-wave (independently estimated) attenuation, and no stations record substantial anticorrelation between Δt^*_S and Δt^*_P. However, when averaging across the entire data set there is no statistically significant correlation between individual or station-

21699356, 2025, 2, Downloaded from https://agupubs.onlinelibrary.wiley.com/doi/10.1029/2024JB030417 by University Of California Santa Barbara, Wiley Online Library on [14/02/2025]. See the Terms and Conditions (https://onlinelibrary.wiley.com/terms-and-conditions) on Wiley Online Library for rules of use; OA articles are governed by the applicable Creative Commons License

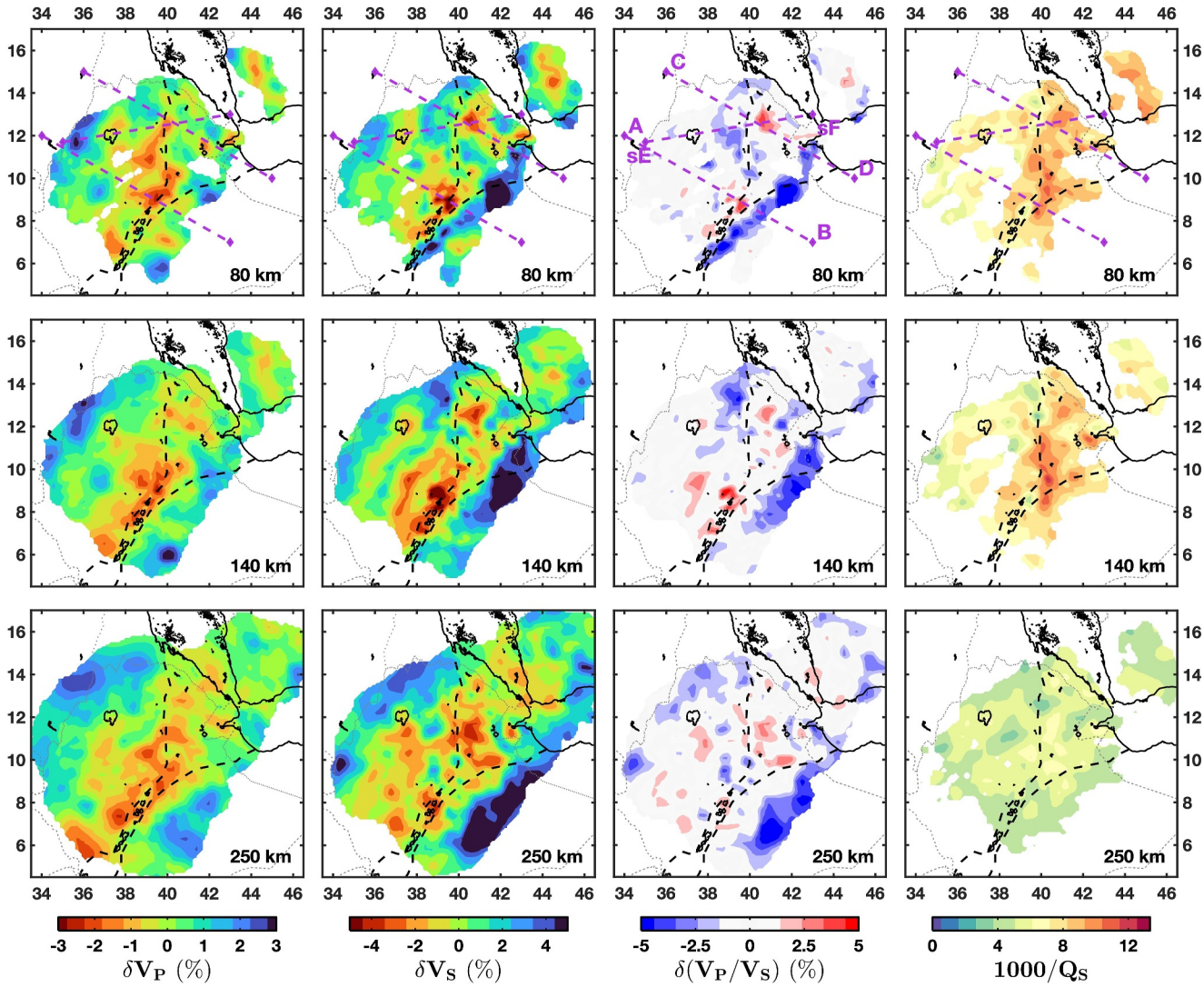


Figure 5. Horizontal slices through the velocity and shear attenuation tomography models, showing percentage deviations in properties from the layer averages. Black dashed line is hand-drawn boundary of the East African Rift and Afar depression based on topographic expression. Light dotted lines are political boundaries. Magenta dashed lines in the top row show the locations of cross-sections in Figures 6 and 7, and S21.

averaged Δt^* measurements (Figure 4). Breaking the trends down by sub-regions, no significant Δt_S^* versus Δt_P^* correlation is found on the Plateau or the rift axis. The Plateau region stands out for having a similar spread in amplitudes of Δt_P^* than in Δt_S^*, though the measured attenuation here is not high and P-S correlation is not significant. In Afar, however, the station average Δt^* values *do* show signs of positive correlation between *P* and *S* ($R^2 = 0.45$) and the ratio of maximum to minimum eigenvalues (indicative of linear data trends) is 4.0 (it would be <2.5 for uncorrelated data, accounting for differences in measurement error). For these data, the PCA-estimated $\Delta t_S^*/\Delta t_P^*$ slope is 2.91.

4.2. Tomographic Models

Together, the tomographic velocity and attenuation models (Figures 5–7, Figures S15–S21 in Supporting Information S1) provide a new dimension of imaging of the MER, Afar, and the rift flank. The velocity structure of this region has been comprehensively studied using a number of methods and data types (Bastow et al., 2005, 2008; Benoit, Nyblade, & Pasyanos, 2006; Boyce et al., 2021; Chambers et al., 2019, 2022; Civiero et al., 2015, 2016; Eshetu et al., 2021; Hammond et al., 2013; Hansen & Nyblade, 2013; Keranen & Klemperer, 2008; Kounoudis et al., 2021). The δV_P and δV_S models achieve high weighted data variance reductions of 90.3% and

21699356, 2025, 2, Downloaded from https://agupubs.onlinelibrary.wiley.com/doi/10.1029/2024JB030417 by University Of California Santa Barbara, Wiley Online Library on [14/02/2025]. See the Terms and Conditions (https://onlinelibrary.wiley.com/terms-and-conditions) on Wiley Online Library for rules of use; OA articles are governed by the applicable Creative Commons License

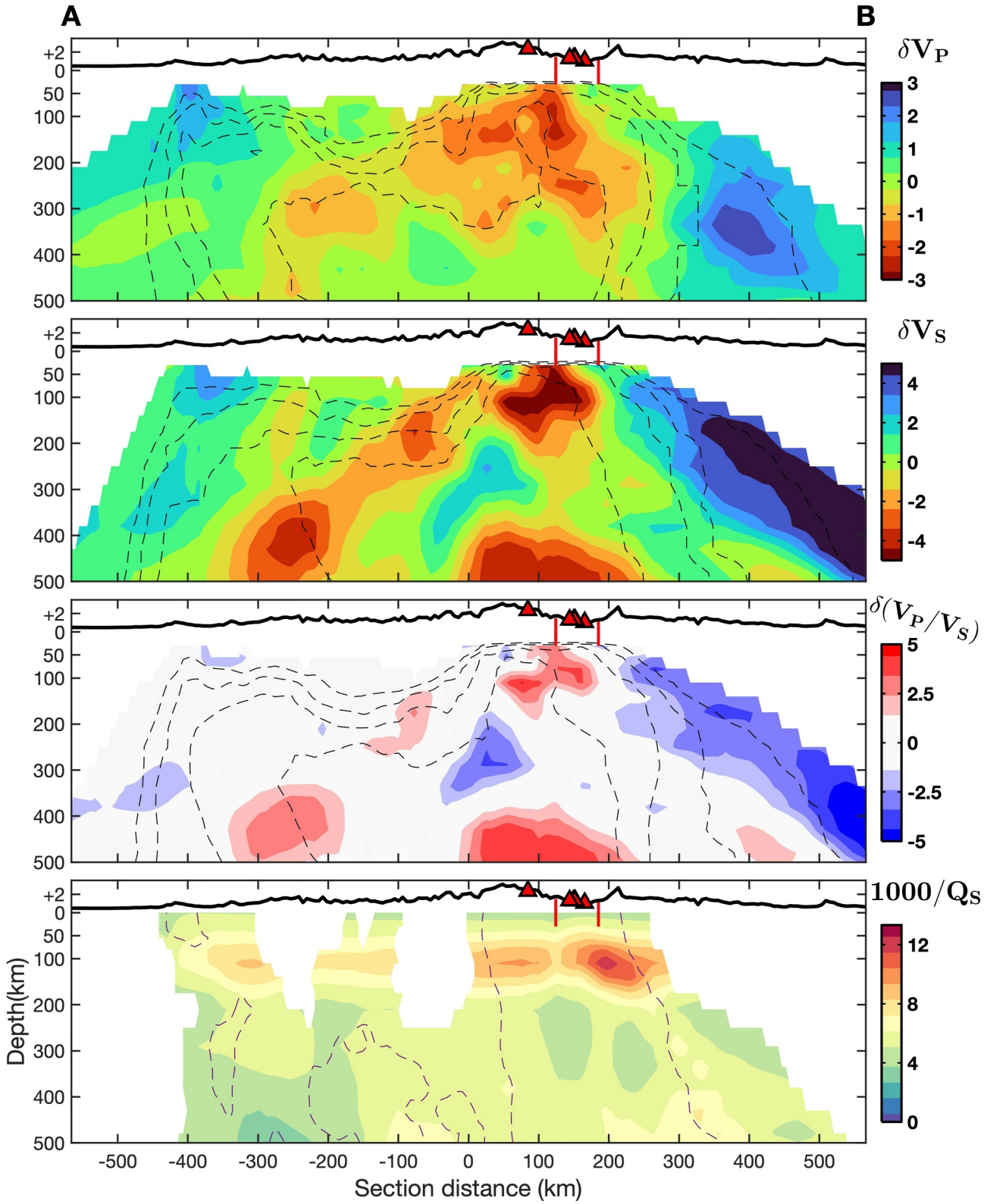


Figure 6. Vertical slices through the velocity and attenuation tomography models along cross-section A–B, showing percentage deviations in properties. Structure is masked out for model nodes with "hit quality" below 0.1. Black dashed lines are 0.6, 0.7, 0.8, and 0.9 hit quality contours. Topography is plotted with 20x vertical exaggeration. Red triangles are volcanoes within 50 km of the section, projected onto the section. Red lines are boundaries of the surface expression of the East African Rift.

21699356, 2025, 2, Downloaded from https://agupubs.onlinelibrary.wiley.com/doi/10.1029/2024JB030417 by University Of California Santa Barbara, Wiley Online Library on [14/02/2025]. See the Terms and Conditions (https://onlinelibrary.wiley.com/terms-and-conditions) on Wiley Online Library for rules of use; OA articles are governed by the applicable Creative Commons License

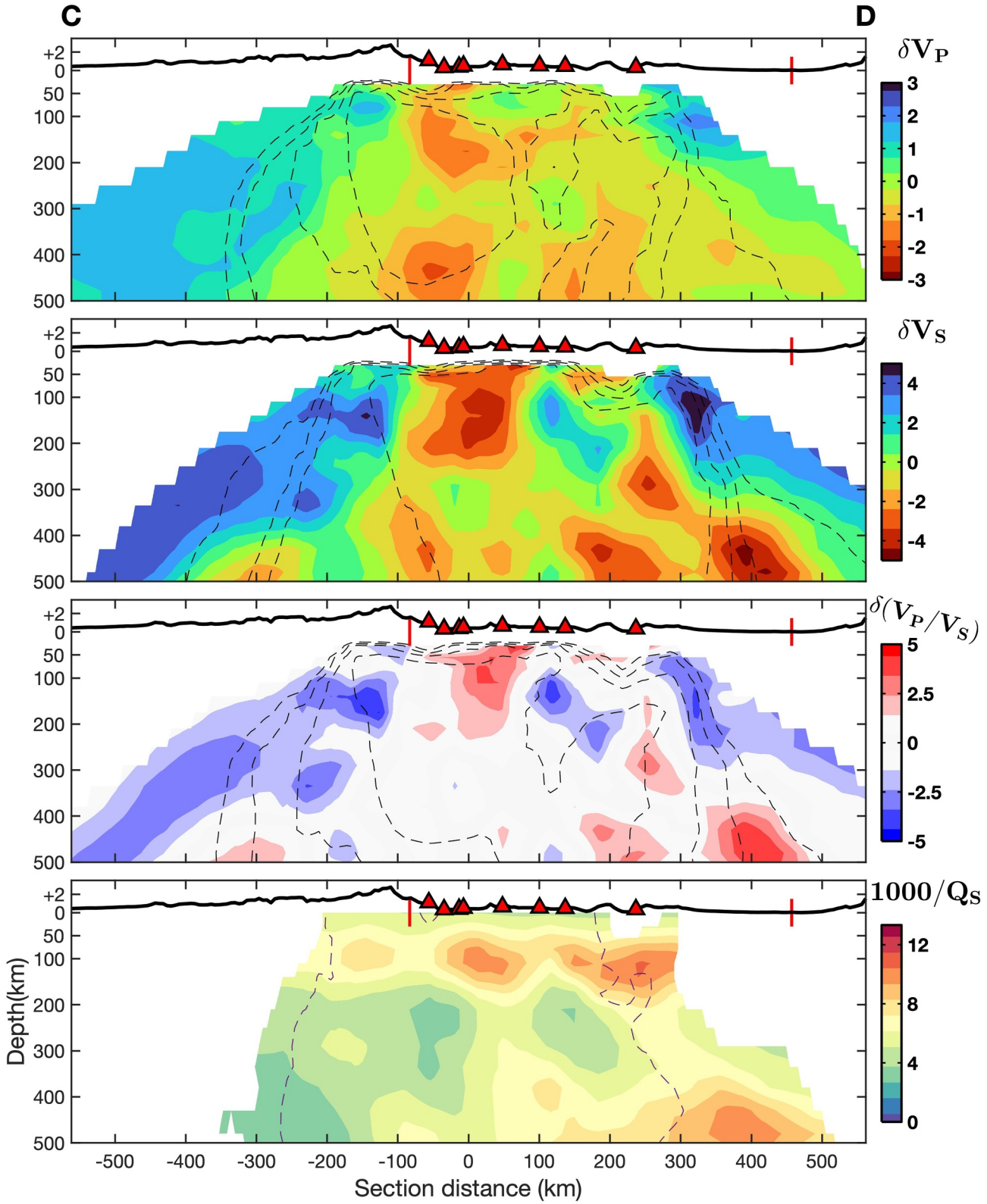


Figure 7. As for Figure 6 but showing vertical slices along cross-section C–D. Red lines are edges of the Afar triangle.

21699356, 2025, 2, Downloaded from https://agupubs.onlinelibrary.wiley.com/doi/10.1029/2024JB030417 by University Of California Santa Barbara, Wiley Online Library on [14/02/2025]. See the Terms and Conditions (https://onlinelibrary.wiley.com/terms-and-conditions) on Wiley Online Library for rules of use; OA articles are governed by the applicable Creative Commons License

21699356, 2025, 2, Downloaded from https://agupubs.onlinelibrary.wiley.com/doi/10.1029/2024JB030417 by University Of California Santa Barbara, Wiley Online Library on [14/02/2025]. See the Terms and Conditions (https://onlinelibrary.wiley.com/terms-and-conditions) on Wiley Online Library for rules of use; OA articles are governed by the applicable Creative Commons License

85.4%, respectively. The RMS residuals are 0.23 s for ΔT_P, and 0.63 s for ΔT_S. δq attenuation models have lower weighted data variance reduction: 49.7% and 48.8%, respectively for P and S. This is due to noisy data: RMS residuals are 0.23 s for P and 0.41 s for S. To explore the statistical significance of these inversion results, I conducted a "null hypothesis" test whereby random data with the same standard deviation as the true data was tomographically inverted with the same regularization. This "null" inversion (repeated 200 times to obtain bootstrapped statistics) achieved a variance reduction of 28.0 ± 1.4%, for δq_S (the lowest variance reduction inversion), well below the true data variance reduction (Figure S5 in Supporting Information S1). This test demonstrates that although the fraction of Δt^* variance fit is much lower than that of ΔT, the *worst* fit is still 15.3 standard deviations higher than random, and the attenuation models are meaningful.

4.2.1. Model Resolution and Reliability

Checkerboard tests (Figures S7–S14 in Supporting Information S1) indicate excellent model recovery for velocity tomography, and good model recovery for δq_S models at a feature scale of ∼200 km throughout the Afar and between the MER and eastern border of Ethiopia, throughout the vertical extent of the models. These inversions include synthetic noise on the order of that observed in the real data (estimated a posteriori from the real data inversion residuals), so capture both the effects of stochastic error and of resolution limitations due to the structure of the data kernels. Finer checkerboard inversions indicate that velocity tomography has very good resolution down to <100 km scale, best beneath the rift flank and the rift axis (but not in between) at shallower depths. δq_S models have adequate 100 km resolution (at best) only at shallow depths and mostly beneath and adjacent to Afar and the MER. Downwards smearing of checkers toward the edge of the models, where the hit quality (a combined measure of hit count and back-azimuthal coverage; Eilon et al., 2015) contours indicate deteriorating ray coverage, demonstrates that we should be skeptical of the depth extent of structures appearing at the edges of models. In this region, the lithosphere is largely thought to be thinner than ∼80 km (Bastow et al., 2010; Dugda et al., 2007; Petruska & Eilon, 2022; Rychert et al., 2012). The synthetic tests indicate that the inversion may map some truly lithospheric-scale heterogeneity to slightly deeper model depths (<200 km). This type of smearing is inevitable for steeply dipping teleseismic body waves, yet may be exaggerated by the alternating checker structure.

δq_P synthetic structures are poorly recovered (Figures S9 and S14 in Supporting Information S1). This stems from the fact that the starting models assume essentially no attenuation in bulk ($Q_\kappa = 943$), in accordance with 1-D mantle models (Durek & Ekström, 1996), and with consequently low sensitivity to Q_P the tomography fails to recover input structure in the presence of realistic synthetic data noise. The $\Delta t_S^*/\Delta t_P^*$ observations are not supportive of small bulk attenuation, since that would imply much smaller values of Δt_P^* than recorded. However, since it is not clear what starting Q_κ is reasonable, and since our community currently lacks robust laboratory constraints on the systematics of bulk mantle attenuation, I provide the δq_P models for the interested reader in the supplement (Figure S17 in Supporting Information S1) but do not focus on them in the main text.

"Spread" or "spike" tests roughly depict rows of the model resolution matrix corresponding to the locations of the input spikes (Figures S31–S42 in Supporting Information S1). These tests are conducted with no synthetic noise, to isolate intrinsic data resolution limitations. These tests reveal no preferential direction of horizontal smearing. Small sidelobe artifacts appear in some of the models, particularly for the Plateau-centered spike. These arise from the first-derivative flattening. A limited amount of vertical smearing is observed, but shapes are preserved well, at least in the uppermost 300 km.

All recovery tests reveal quite substantial amplitude reduction in recovered structure. This is common for damped inversions, and difficult to avoid given the need for damping in the presence of noisy data. Imaged anomalies may underestimate true heterogeneity amplitudes. Comparing spikes in different locations indicates that attenuation amplitude reduction is least problematic in the north MER (Figure S38 in Supporting Information S1). Overall, the amplitude reduction is much more marked for attenuation than for velocity. To account for this when jointly interpreting q_S and V_S, I use the checkerboard tests to compute an amplitude loss factor (Figure S29 in Supporting Information S1); this factor is used to multiply the models used for the thermodynamic interpretation, but not for any of the "raw" tomography results presented below.

21699356, 2025, 2, Downloaded from https://agupubs.onlinelibrary.wiley.com/doi/10.1029/2024JB030417 by University Of California Santa Barbara, Wiley Online Library on [14/02/2025]. See the Terms and Conditions (https://onlinelibrary.wiley.com/terms-and-conditions) on Wiley Online Library for rules of use; OA articles are governed by the applicable Creative Commons License

4.2.2. Velocity Models

The clearest feature in the velocity models (Figures 5–7, Figures S15, S16, and S20 in Supporting Information S1) is the slow MER rift axis. Slow velocities are highly asymmetric about the rift at depth. At (sub-)lithospheric depths (~50–200 km), the transition to fast off-rift material southeast of the rift is sharp, over less than 100 km distance, but more gradual beneath the Ethiopian Plateau, where faster-than-average lithospheric velocities only appear ~450 km NW of the rift bounding fault (Figure 6). At lithospheric depths (<100 km deep) a concentrated region of particularly low velocity is observed at around 8–10°N centered between the border faults. Another zone of low P and S velocity is seen at 11°N, about 80 km west of the Afar triangle, outside of the obvious surface expression of extension. Within the Afar itself, A NW-SE zone of moderately faster velocities separates the slow velocities at the base of the triangle from another zone of slow velocities at ~40–42°E that runs sub-parallel to the coastline. At greater depths (100–250 km), low velocity structure extends further westward, to Lake Tana (Figure S21 in Supporting Information S1). Another localized region of slow V_S and V_P coincides closely with Lake Tana itself. West of the rift, models reveal one or possibly two slow lineaments running SSW-NNE, sub-parallel to the main rift, although these features are more apparent in δV_S. Still deeper (>260 km), the entire Afar depression is slow, with lowest velocities (cross-section C–D; Figure 7) beneath its center. Vertical cross sections show that low velocities beneath the rift axis are deep-seated (Figure 6). A broad, deep zone of low velocity (both compressional and shear) narrows upwards toward the rift axis, albeit asymmetrically, with greater breadth to the northwest.

Co-located P and S models allow us to evaluate relative variation in V_p/V_s ratio: $\delta(V_p/V_s)$ (see Text S2 in Supporting Information S1) (e.g., Koulakov et al., 2020). This value is a proxy to discriminate temperature-controlled velocity change (zero or negative value) from more melt-dominated change (high values, indicating preferential shear modulus depression). In the shallower parts (<140 km depth) of the model where the association with melt, specifically, may be more robust, high $\delta(V_p/V_s)$ is mostly confined to the MER axis (section A–B), the northern Afar in a line perpendicular to Red Sea spreading (sections C–D, sE-sF), and a small region near Lake Tana (Figure S21 in Supporting Information S1). At intermediate depths (150–300 km), high values of this parameter are more distributed west of the rift axis, but the eastern boundary of the elevated $\delta(V_p/V_s)$ is clearly defined. At greater (>300 km) depth, northern Afar again shows up as a region of high $\delta(V_p/V_s)$ as does the southern MER toward Turkana.

4.2.3. Attenuation Models

The S-wave attenuation model (Figure 5, Figures S18 and S19 in Supporting Information S1) shows high differential attenuation in the region of the rift axis, and particularly along the western edge of the Afar triangle, similar to where we find lowest shear velocities. High attenuation is also found in the shallower mantle (<150 km) in the vicinity of Lake Tana. Unlike the velocity tomography, the attenuation models do not demarcate very obvious boundaries to the rift, though the attenuation values seen beneath the Arabian peninsula and southwest of the MER are markedly lower than the high attenuation seen within the rift.

The attenuation model contains some unexpected structures. Beneath the center of the rift axis, at [8.3°N, 39.2°E], a small but strong region of *negative* apparent differential attenuation is seen extending down to ~200 km (Figure 5, Figure S18 in Supporting Information S1), despite this being close to the locus of the *minimum* seismic velocities. This feature is mimicked in the less robust (but independently inverted) δq_P models (Figure S17 in Supporting Information S1), and coincides with active volcanoes (e.g., Di Paola, 1972; Wolfenden et al., 2004). Meanwhile, the highest attenuation close to the northern MER, at ~8.7°N, seems to be displaced slightly (~50 km) east of the axis itself, and apparently dips from the rift down to the east, though this may not be well resolved. To the west of the rift, a broad zone of higher attenuation extends westward from the rift axis at ~9°N at shallower (<150 km) depths. This feature roughly matches a high $\delta(V_p/V_s)$ zone, but runs roughly perpendicular to apparent lineaments in low δV_S. Deeper than 200 km, large regions of the center of the study area, particularly beneath Afar and west of the MER axis, are found to be highly relatively attenuating. That said, since the starting model has relatively low baseline attenuation in these regions, the high fractional perturbations do not translate to very high absolute $1/Q_S$.

21699356, 2025, 2, Downloaded from https://agupubs.onlinelibrary.wiley.com/doi/10.1029/2024JB030417 by University Of California Santa Barbara, Wiley Online Library on [14/02/2025]. See the Terms and Conditions (https://onlinelibrary.wiley.com/terms-and-conditions) on Wiley Online Library for rules of use; OA articles are governed by the applicable Creative Commons License

5. Discussion

5.1. Elastic and Anelastic Structure: Implications for Rift Development

Velocity tomography (Figures 5–7) depicts clear structure that is consistent with previous studies (*e.g.*, Bastow et al., 2008; Boyce et al., 2021; Chambers et al., 2022; Civiero et al., 2015). The rift axis is slow, and low P and S velocities extend asymmetrically off-rift beneath the western Ethiopian Plateau, as far as Lake Tana, a focus of some quaternary volcanism and hydrothermal activity (Figure 1). East of the MER, there is a sharp transition to apparently colder, stiffer structure beneath the Somalian Plateau. This gradient roughly aligns with a step in crustal thickness (Keranen et al., 2009). Low velocities and high $\delta(V_P/V_S)$ ratios indicate melt localized beneath the MER, northern Afar, and Lake Tana. In the center of the rift, a sub-vertical conduit of slow, likely melt-rich material connects the surface to >500 km depth (Figure 6). High apparent temperatures and melt fractions extend in secondary structures that branch under the Plateau. The overarching picture here is of lithospheric deformation and asthenospheric temperature elevation that is highly asymmetrical: sharply bounded to the SE and broadly distributed to the NW. The most attenuating regions are mostly close to the rift axis, but their along-axis extent is highly variable. The two clearest high-attenuation structures in the models are the Afar triangle (where δq models depict deeply rooted attenuation) and the northern MER.

A key result is low velocities, moderately high S-wave attenuation, and highest $\delta(V_P/V_S)$ at apparent depths of 150–350 km in a swath beneath the western Ethiopian Plateau, that imply hot asthenosphere well off-axis. These low velocities may be somewhat smeared downwards from shallower depths, but the data seem to require some relatively faster lithosphere above them. Overall, this is consistent with melt ponded or organized along the base of the lithosphere across a broad region (cf. Holtzman & Kendall, 2010), which could cause lithospheric degradation through impounding and melting (Ferrando et al., 2008; Havlin et al., 2013; Trestrail et al., 2017) responsible for broad weakening and thinning (Lavayssière et al., 2018) of the Plateau lithosphere. A NNE-SSW lineament of V_S reduction and δq_S is found as far west as Lake Tana, spatially consistent with recent volcanism. These results add weight to arguments that off-rift magmatic processes here broaden extension and modulate time-dependent rift dynamics (Chiasera et al., 2018; Keranen et al., 2018; Kumar & Legendre, 2022).

The slowest relative velocities beneath the plateau are relatively deep: 200–400 km (Figure 5). This apparent depth is subject to some error; body waves alone yield poor depth constraints in the mid-upper mantle anomalies. That said, two lines of reasoning suggest the mantle here is slowest at >200 km depth. First, in squeezing tests that limit structure to the upper 200 or 300 km of the model space (Figures S23–S28 in Supporting Information S1), the lowest velocities beneath the Plateau bunch up at the *deepest* un-squeezed layer and overall model fit declines, indicating the data prefer deeper anomalies. Second, absolute shear velocities from surface wave models (Accardo, 2018; Chambers et al., 2019, 2022), and a joint inversion of surface waves and receiver functions in this location (Petruska & Eilon, 2022), suggest elevated but not enormously high temperature (or melt-fraction) sub-lithospheric mantle down to 150 km beneath the Plateau. The presence of melt as deep as 200 km would require volatile modification of the dry mantle solidus and/or elevated mantle potential temperatures (Dasgupta & Hirschmann, 2010; Dasgupta et al., 2013). Both are plausible in the context of plume-charged asthenosphere (Dixon et al., 2008) and the EAR is well known for extensive CO_2 outgassing (Muirhead et al., 2020).

Afar, as expected, has slow velocities and high attenuation. At shallower depth (<200 km) the slowest velocity, highest $\delta(V_P/V_S)$ ratios, and highest attenuation are concentrated along (or even west of) the western edge of the Afar triangle (Figures 5 and 7). This is largely in agreement with previous imaging (Boyce et al., 2021; Chambers et al., 2022; Guidarelli et al., 2011; Hammond et al., 2013), which depicts lower velocities beneath the MER than Afar at depths ≥100 km, despite obviously greater extents of crustal extension at the latter (*e.g.*, Hammond et al., 2011). Moreover, Quaternary volcanism, extension, and seismicity is mostly confined to this side of the depression (Bastow & Keir, 2011; D. Keir et al., 2013; Korostelev et al., 2015). These results indicate that focused upper mantle upwelling aligns with these shallow expressions of extension.

At >350 km depths, slow velocities (particularly δV_S) and high attenuation beneath the northern Afar and Red Sea-Afar-Aden triple junction area dominate the models (Figure 7, Figures S15–S20 in Supporting Information S1). This structure is likely the "Afar" mantle plume tail that has influenced East African breakup since ≥20 Ma (*e.g.*, Civiero et al., 2022). There is clear contiguity between this deep feature and the shallowest expressions of low velocity etc. in the rift. As many others have shown (*e.g.*, Boyce et al., 2021; Civiero et al., 2022; Schilling et al., 1992), this rift has been strongly affected by at least one deep-rooted mantle plume. At depths

21699356, 2025, 2, Downloaded from https://agupubs.onlinelibrary.wiley.com/doi/10.1029/2024JB030417 by University Of California Santa Barbara, Wiley Online Library on [14/02/2025]. See the Terms and Conditions (https://onlinelibrary.wiley.com/terms-and-conditions) on Wiley Online Library for rules of use; OA articles are governed by the applicable Creative Commons License

>400 km, the δV_S model indicates two loci of slow velocities: beneath northern Afar and at the southern MER, in line with previous work (Civiero et al., 2015). The q_S model only has resolution to identify the northern of these putative upwellings, but deep, high absolute q_S at Afar (Figure S19 in Supporting Information S1) aligns well with inferred hydrous upwelling through the transition zone determined using receiver functions (*e.g.*, Thompson et al., 2015). The fact that both velocity and attenuation models depict a plume structure to depth (albeit not identically; Figure 6) suggests that it is not only hot but may contain some deep-sourced carbonatitic melt.

Several workers have previously demonstrated that the EAR is highly segmented, with along-strike (and off-axis) localization of strain and volcanism dictated in large part by pre-existing lithospheric structure (Corti et al., 2018; Kolawole et al., 2021). The models presented here are sensitive to upper mantle features, making direct linkage to detailed crustal segmentation challenging. However, the shallowest well-resolved (80 km) depth slices show a very slow and highly attenuating structure beneath NW Afar (~13°N, 41°E) that matches closely with shallowest Moho and highest crustal V_p/V_s (Ahmed et al., 2022; Hammond et al., 2011) and the most active volcano-seismic segments (Ebinger et al., 2008). At 80 km, two other localized, low-$\delta(V_P/V_S)$ features on the rift axis at ~9°N, 39.5°E and ~7°N, 38°E align with the intersection of the rift axis and the Yerer-Tullu Wellel volcanic lineament (YTVL; Abebe Adhana, 2014) and Goba-Bonga lineament (GBL; Abbate & Sagri, 1980), respectively (Figure 1). These slow velocities, arguably extending westwards along the lineaments beneath the plateau, as seen in other studies (Bastow et al., 2008; Chambers et al., 2022), can be inferred to have very high melt fraction from the high $\delta(V_P/V_S)$ and illustrate how lithospheric deformation manifests an interplay of pre-existing weaknesses and strain-weakening behavior (Corti et al., 2022). The northern of these two structures is arguably seen as high attenuation in the q_S model.

5.2. Physical Conditions of the MER

A primary motivation of this study was to combine velocity and attenuation structure to elucidate physical conditions of the mantle within and adjacent to the rift. I link shear velocity and attenuation to temperature, melt fraction, pressure, grain size, composition, and frequency, use laboratory-derived expressions within the self-consistent framework of the Very Broadband Rheology calculator (VBRc, Havlin et al., 2021; Lau et al., 2020). For depths of 80–140 km, I construct look-up tables ("*LUT*") of predicted V_S and Q_S on a dense grid of sought-after parameters: temperature [T: 800–1,600°C], melt fraction [ϕ: 0%–3.16%; log-spaced], and grain size [d: 31μm–31 mm; log-spaced]. I use the calculator of Abers and Hacker (2016) to obtain anharmonic elastic moduli and densities, assuming a lherzolitic contribution (ignoring volatiles), and then account for melt via the poroelastic effect (Takei, 2002). I adjust for physical dispersion and calculate predicted shear attenuation using the scaling of Yamauchi and Takei (2016) which includes the "pre-melting effect" and direct melt effects on anelasticity (Holtzman, 2016; Yamauchi & Takei, 2024). The exact effect of melt on observable seismic parameters is complex, disputed, and may depend heavily on geometry and connectivity (Faul et al., 2004; Freitas et al., 2019; Hammond & Humphreys, 2000a, 2000b; Holtzman, 2016; McCarthy & Takei, 2011; Shankland et al., 1981; Takei, 2017). The approach I take above results in melt much more strongly reducing velocities than it does increase shear attenuation (Havlin et al., 2021), and does not explicitly invoke phenomena such as melt squirt (Mavko & Nur, 1975; O'Connell & Budiansky, 1977) or wave-induced freezing/unfreezing (Vaišnys, 1968). These LUTs, along with priors on state variables, are used to invert for state variables in a Bayesian framework in a fashion similar to previous work (Havlin et al., 2021; Lau et al., 2021; Paxman et al., 2023); more details can be found in the supplement (Text S3 in Supporting Information S1).

I invert averaged V_S and $1/Q_S$ within several regions of interest (Figure 8, Figure S30 in Supporting Information S1). These regions are hand-picked to reflect contiguous areas that (a) have interpretation value, (b) have similar internal structure in V_S and $1/Q_S$, (c) are well resolved according to the synthetic tests. Two caveats must be acknowledged: First, I invert the *median* seismological parameters in each region, not point-by-point values. Variation in individual V_S and $1/Q_S$ values makes these too large to be easily interpreted. The drawback of this approach is that only average outputs (state variables) can be interpreted. The benefit is that anomalous local model features (*e.g.*, a possible focusing attenuation artifact within the *NMER*) do not overly bear on the results. Second, there is uncertainty in calculating absolute V_S and $1/Q_S$ values from the *perturbational* inversions obtained from differential data. I convert from perturbational values to absolute values using global models: a local 1-D average of 18 global Versus models from SubMachine (Hosseini et al., 2018), and the 3-D QsADR17 model for Qs (Adenis et al., 2017). Following Shinevar et al. (2023), I scale up the δq_S values to account for tomographic amplitude loss, as described in Section 4.2.1. and Figure S29 in Supporting Information S1. Given these caveats, a

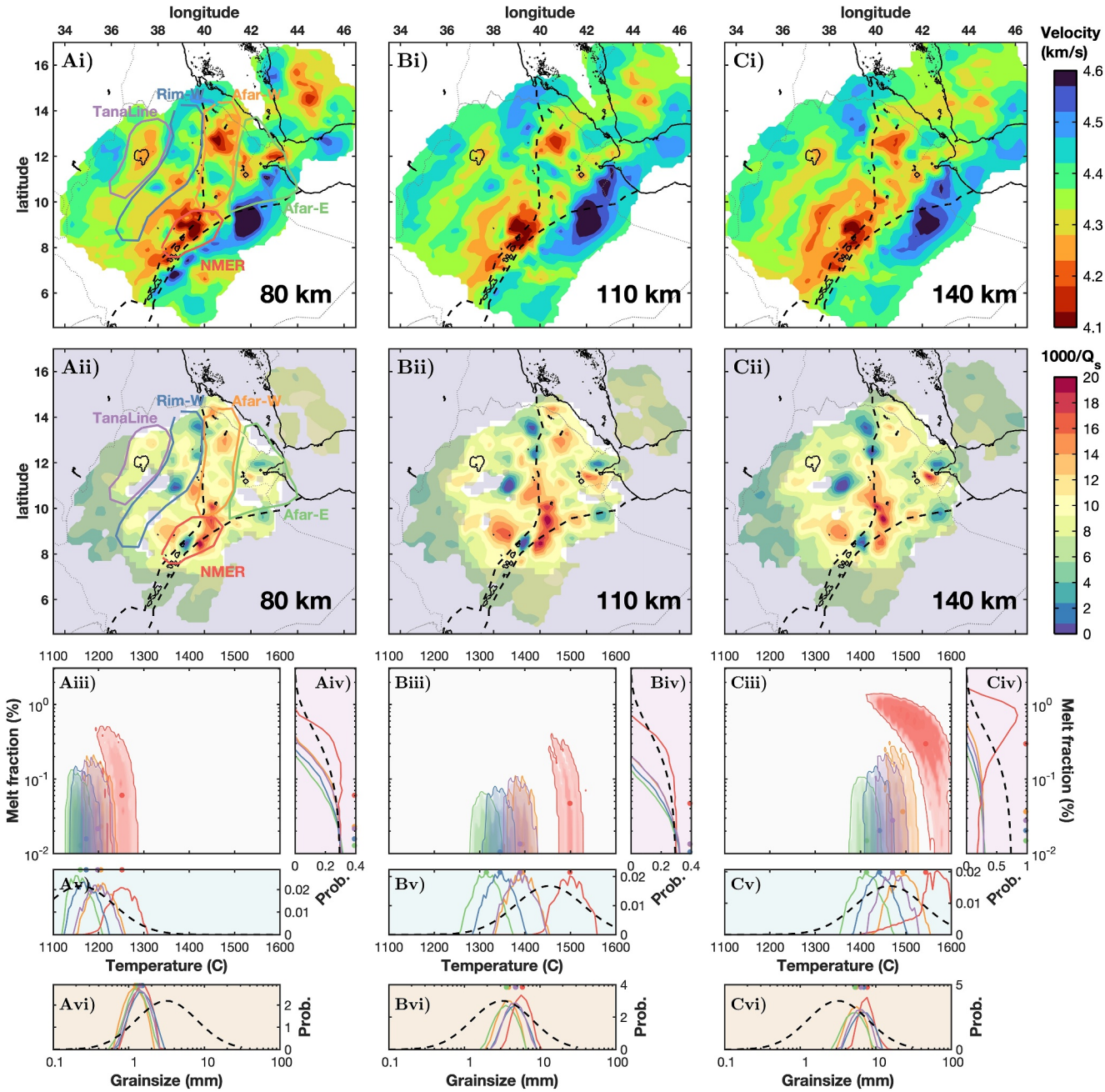


Figure 8. Regional inversions for state variables from seismic observables. Within five regions of interest, outlined in (Ai, Aii) and denoted throughout by color, median values of absolute shear velocity (i) and attenuation (ii) are inverted for Temperature, melt fraction and grain size at three different depths (A = 80 km; B = 110 km; C = 140 km) using a Bayesian approach as described in the text. Note that attenuation is scaled to account for inversion amplitude loss (Section 5.2). (iii) Panels show the bivariate pdf of temperature and melt fraction (note the log scale for the latter), with shaded contours demarcating 0.5 (bold line), 0.55, 0.75, 0.9, 0.95 of the maximum posterior probability. Univariate pdfs for melt fraction, temperature, and grain size are in panels (iv), (v), and (vi), respectively, along with the priors (black dashed lines). Small dots in (iii–vi) show expected (not maximum likelihood) values of the variables.

cautious reader may prefer to rely on contrasts in, rather than absolute values of, inferred thermodynamic properties described below.

The inversions place quantitative bounds on mantle conditions, with uncertainties (Figure 8 and Table S1 in Supporting Information S1). At 80 km depth, all regions sit just below the adiabat (for a 1,300°C potential temperature), and are on or above this adiabat by ~110 km depth. This is in close, but not precise, alignment with

21699356, 2025, 2, Downloaded from https://agupubs.onlinelibrary.wiley.com/doi/10.1029/2024JB030417 by University Of California Santa Barbara, Wiley Online Library on [14/02/2025]. See the Terms and Conditions (https://onlinelibrary.wiley.com/terms-and-conditions) on Wiley Online Library for rules of use; OA articles are governed by the applicable Creative Commons License

21699356, 2025, 2, Downloaded from https://agupubs.onlinelibrary.wiley.com/doi/10.1029/2024JB030417 by University Of California Santa Barbara, Wiley Online Library on [14/02/2025]. See the Terms and Conditions (https://onlinelibrary.wiley.com/terms-and-conditions) on Wiley Online Library for rules of use; OA articles are governed by the applicable Creative Commons License

other data sets indicating the lithosphere here is everywhere ≤80 km thick (Bastow et al., 2010; Dugda et al., 2007; Petruska & Eilon, 2022; Rychert et al., 2012). The hottest and most melt-laden region, at all depths from 80 to 140 km, is the northern MER (*NMER*) region. At 80 km depth, I infer a temperature here of ∼1,250°C, placing it nearly on the adiabat and supporting the proposition that axial lithosphere is particularly thin (Dugda et al., 2007; Rychert et al., 2012). In addition, consequential amounts of in situ melt (on average ∼0.1% but up to ∼0.5%) are inferred here, consistent with rift volcanism (Rooney, 2020). At greater depths, the inversion suggests this region is hot, with mean temperatures of ≥1,500°C (albeit with some melt tradeoff) that translate to mantle potential temperatures ≥1,450°C, comparing favorably to petrological estimates of 1,420–1,460°C from <10 Ma extrusives here (Rooney et al., 2012). Taken at face value, the *NMER* has higher fractions of melt with increasing depth, with a maximum ∼0.3% (but up to 1.2%, within error) at 140 km depth. This positive trend is the opposite of what we might expect given the pressure control on melting (*e.g.*, Hirschmann, 2000), though is consistent with other studies that echo this inversion approach (Paxman et al., 2023). It may be that melt channelization and extraction is more established and efficient at shallower depths, leading to less in situ melt to which seismic waves are sensitive. Alternatively, a change in melt geometry could explain this variation (cf. Hammond & Kendall, 2016); the geometry is assumed to be constant in the Bayesian analysis. Melt at >100 km depth would be enhanced by volatiles (Dasgupta et al., 2013; Hirschmann, 2006), likely supplied by the plume(s) (Dixon et al., 2008; Halldórsson et al., 2022). Such deep melt should be relatively depleted in heavy rare earth elements and, although this could be swamped by shallower melting, this geochemical pattern has been seen in East Africa–in Afar (Ferguson et al., 2013). Finally, the *NMER* seems to have moderately larger grain sizes than elsewhere, perhaps driven by grain growth kinetics at higher temperatures (Austin & Evans, 2007; Dannberg et al., 2017).

The *TanaLine* and *Afar-W* regions show many similarities, despite the former being ostensibly away from the locus of rifting. Both regions are hot at shallow depths (∼1,200°C at 80 km, ∼1,380°C at 110 km) and have appreciable melt fractions of up to 0.1%. At 140 km depth, the western Afar seems to have modestly higher temperature than the Tana lineament (∼1,490°C vs. 1,470°C) corresponding to the ∼25% greater attenuation and slightly lower velocity. These temperatures are also close to previous estimates for Afar (*e.g.*, Armitage et al., 2015). At all depths, *Afar-W* has moderately smaller grain sizes than *TanaLine*, perhaps reflecting some greater concentration of strain rate (Austin & Evans, 2007). *Rim-W* and *Afar-E* have the highest velocities and lowest attenuation, and are consequently inferred to be the coolest and least melt-saturated regions. Despite this, they are warm compared to an average geotherm; their 140-km-depth temperatures of ∼1,440°C and 1,410°C, respectively, lie between the adiabats for 1,350°C and 1,400°C potential temperatures. As others have found, the entire upper mantle is hot here.

Taken together, these results imply regional heterogeneity in rifting maturity and active deformation. As expected, the northern MER is a particular focus of extension and high temperature. Further north, we see a large difference between eastern and western Afar; upper mantle active upwelling and melting is localized in the western portion of this broad topographic low. The flank region at and SSW of Lake Tana is the next-most "mature", with apparently higher temperatures and greater melt fractions than the central Ethiopian Plateau (*Rim-W*). Although the western extent of rifting is broadly distributed, it is not universally so—some process seems to be localizing off-axis deformation preferentially beneath the western Plateau.

5.3. Comparisons Among Data Types

The correspondence between *P* and *S* travel times and velocity models is extremely good (Figures 3, 5–7, Figures S15 and S16 in Supporting Information S1). Disagreements are found only in model details, such as the δV_S model depicting more lineated rift-parallel slow structures beneath the western Ethiopian highlands than δV_P, and also having more concentrated zones of slow velocities at >400 km depth. Travel time ratios (Section 4.1.1.) indicate a melt-dominated MER ($\mathrm{d}\ln V_S/\mathrm{d}\ln V_P \approx 2.19$), concurring with velocity models that depict $\delta\left(\frac{V_P}{V_S}\right) > 3\%$ at shallower depths within the rift axis. In the northwest Afar, resolved well in all models, we see agreement among all tomographic models. For instance, at <150 km depth, a patch of high δq_S at [13°N, 41°E] that is clearly separated from less attenuating material to its west and southeast is echoed precisely by an isolated slow velocity and high-$\delta\left(\frac{V_P}{V_S}\right)$ structure.

Elsewhere, velocity-attenuation correspondence is mixed. Strong attenuation along the southwestern edge of Afar is not clearly mirrored in the velocity models, though it does resemble maps of most-delayed station-averaged ΔT.

21699356, 2025, 2, Downloaded from https://agupubs.onlinelibrary.wiley.com/doi/10.1029/2024JB030417 by University Of California Santa Barbara, Wiley Online Library on [14/02/2025]. See the Terms and Conditions (https://onlinelibrary.wiley.com/terms-and-conditions) on Wiley Online Library for rules of use; OA articles are governed by the applicable Creative Commons License

The clearly demarcated SE boundary of the rift axis is not well observed in attenuation models. As noted above, a localized zone of apparently *negative* attenuation at 80–150 km depth within the rift axis [8.3°N, 39.2°E] paradoxically coincides with some of the slowest velocities and surface volcanism. This is surely a localized wave-focusing structure that somehow persistently escaped the focus-test QC. Most surprising is uneven agreement between upper (140–300 km) mantle attenuation and velocity in the MER itself. The MER upper mantle is hot and melt-ridden, and temperature should exert primary control on attenuation. A reasonable null hypothesis, therefore, is that this rift should manifest high differential attenuation all along the rift axis at relatively shallow depths. This simple pattern is *not* observed. One possibility is that this is because the entire region is highly attenuating, so differential measurements cannot discriminate "high" from "very high" absolute t^*. This would require the eastern flank to be much seismically faster than the rift but similarly attenuating, which is unlikely (though see below regarding asymmetry in t^* in high-Q regions). Another explanation is that wave focusing by the slow rift erases intrinsic attenuation. However, only a few highly localized regions seem to evince this (see above) and overall the Δt^* data set has passed quality controls directly targeting this possibility. Finally, this surprising observation is not alone: other recent results have shown negligible seismic attenuation even in regions with extremely low velocities and high presumed melt content, such as Yellowstone (Oliveira & Bezada, 2023). Our community may have to reckon with a decoupling of high attenuation and low anharmonic moduli that challenges prior expectations. It bears mentioning that the 0–300 km squeezed tomographic models (Figures S23–S28 in Supporting Information S1) show markedly better correspondence between velocity and attenuation structures, especially between high $\delta\left(\frac{V_P}{V_S}\right)$ and high δq_S (Figures S27 and S28 in Supporting Information S1). Perhaps some aspects of disagreement between the models are artifacts of the starting model or regularization. As an additional complication, new results indicate that shear attenuation may be itself anisotropic; Asplet et al. (2024) demonstrate azimuthally varying *S*-wave t* "splitting" at a station in the MER, attributing this phenomenon to aligned fluid-filled cracks. In the present study, I assume attenuation isotropy, and back-azimuthal variation is connected tomographically to lateral heterogeneity alone. If fluid-caused attenuation anisotropy is strong, it would explain some fraction of the misfit in this inversion, and might slightly bias both attenuation and velocity models (particularly within the rift axis).

A final reason for discrepancy may be that t^* is insensitive to very high-Q regions due to an inherent asymmetry in intrinsic attenuation–waves can only become more attenuated. As Quality factor increases beyond an already high value, an un-attenuated wave cannot become *less* attenuated. This is not the case for velocity and travel time; Earth materials are sufficiently similar in their elastic moduli that relative increases and decreases in slowness produce clearly faster or slower arrivals.

Across the entire field region, Δt_P^* and Δt_S^* are not well correlated (Figure 3). Some of this incoherence is due to noise in the measurements. However, the less-noise-prone station-averaged values indicate surprisingly large Δt_P^* relative to Δt_S^* at the positive (more attenuating) end of the measurements. In particular, stations on the western Ethiopian plateau record similar Δt_P^* and Δt_S^*, each ∼0.25 s (star symbols in Figure 3), in a geographically coherent pattern. Assuming attenuation only in shear, Q_P/Q_S should be 2.25. Given a V_P/V_S ratio of 1.8, we would expect $\Delta t_s^*/\Delta t_P^*$ of approximately 4, *not* unity. These observations seem to flout the assumption of attenuation only in shear and are suggestive of some amount of bulk attenuation. A few studies have argued for high bulk attenuation in select locations (Durek & Ekström, 1995; Stachnik et al., 2004; Wei & Wiens, 2020), though this can be ruled out globally (Durek & Ekström, 1996; Heinz et al., 1982). Theoretical studies have suggested bulk attenuation is linked to the presence of melt, though the relevant relaxation timescales and dissipation strength may be strongly dependent on pore geometry (Budiansky & O'Connell, 1980; Mavko, 1980; Schmeling, 1985). Perhaps the conditions of the upper mantle beneath the Ethiopian plateau (some melt, hypothesized lithospheric impounding, intermediate-high temperatures) combine to more strongly activate mechanisms of bulk attenuation, but this explanation is ad hoc. These data cannot more precisely determine causal mechanisms, nor explain why this region would be so special given its similarity to other parts of the extended rift.

Finally, some limitations of the attenuation tomography are important to acknowledge: There is uncertainty in the (global) reference Q model (Section 3.2) and we use more simplistic sensitivity kernels than for velocities. Large δq perturbations may lead to breakdown of some assumptions of perturbational tomography, and non-linear effects may become important, though unlikely to drastically alter spatial patterns of δq. To address these issues, future work beyond the scope of this study could involve: (a) Alliance of teleseismic Δt^* measurements with high-resolution surface wave data to tie in a local absolute Q reference model. If deep local seismicity exists,

absolute t^* measurements could also assist. (b) Iterative inversions with three-dimensional reference models to account for large perturbations to the starting model (e.g., Salas Pazmino & Eilon, 2024). (c) Development of more sophisticated differential attenuation kernels, using adjoint methods with spectral element approaches or other. (d) Continued development of Δt^* measurement methods, including those combining multiple approaches as a mechanism for QC (Bezada et al., 2019).

6. Conclusions

This study harnesses co-located *P*- and *S*-wave travel time and differential attenuation measurements to obtain 3-D velocity and attenuation tomography models for the northern East African Rift. These models provide an unprecedented multi-modal view of the Main Ethiopian Rift (MER) from its axis to the western Ethiopian Plateau and throughout Afar. Travel times and velocity models depict a slow rift that, while focused near the MER axis, also includes several slow offshoots beneath the Ethiopian plateau, particularly coincident with volcanic activity around and south of Lake Tana. High attenuation is concentrated in the northern MER axis and along the western edge of Afar. Both data sets detect the presence of a deep-rooted Afar plume. Velocity models imply that melt underlies much of the rift axis and parts of the Plateau, raising the possibility that distributed extension is facilitated by melt degrading the base of the Plateau lithosphere. By comparing velocity and attenuation, this study places new constraints on the physical conditions of the rift, with excess mantle potential temperature of ~100°C within the rift (along with substantial melt), and up to ~50°C beneath the Plateau. The distal Plateau manifests higher "rift maturity" than the central Plateau, raising the possibility that new sub-parallel rift branches are in the process of being established. Notwithstanding several improvements in the method to measure high-quality teleseismic attenuation, some aspects of attenuation signals are hard to interpret, possibly owing to attenuation in bulk that disrupts expected compression/shear attenuation ratios.

Data Availability Statement

All data used for this study is openly available via the EarthScope DMC under the network codes 2H (D. Keir & Hammond, 2009), AF (Penn State Univ., 2004), XI (Nyblade, 2000), XW (Leroy et al., 2009), Y6 (K. Keir & Ayele, 2016), YQ (D. Keir et al., 2017), YR (Levèque, 2010), YY (Keranen, 2013), ZF (University of Bristol, 2007), G (IPGP & EOST, 1982), IU (Albuquerque Seismological Laboratory/USGS, 1988), GE (GEOFON Data Centre, 1993) and XJ, XM, YJ, for which no DOI is available but which are all associated with the EAGLE experiment (Bastow et al., 2011). Additionally, data was queried from networks 4H, 5H, Y1, YZ, ZE, ZK, but no measurements from these networks were used in the final data set due to inadequate data number or quality. ΔT and Δt^* measurements and tomographic models presented in this manuscript are available via Dryad repository (Eilon, 2024).

Acknowledgments

This work was funded by NSF Grants EAR-1723170 and EAR-2218695. This work benefited from conversations with Geoffrey Abers, Cristhian Salas Pazimino, Jon Petruska, Jim Gaherty, and Josh Russell. Thanks to Kade Keranen for getting me involved in East Africa. I am very grateful to the many field teams and dedicated PIs who have worked on East African seismology for decades, for providing our community with a wealth of seismic data to study this intriguing region. In particular, this study owes a debt to local scientists in Ethiopia, Kenya, Eritrea, Yemen, and Djibouti for participating in and facilitating field campaigns and data analyses. Among those who have generously shared data and discussed this region with me, I acknowledge (in no particular order), Andy Nyblade, James Hammond, Atalay Ayele, Ian Bastow, Cynthia Ebinger, Derek Keir, Eve Daly, Kade Keranen, Sisay Alemayehu, and J.M. Kendall. The author declares no conflicts of interest for this work.

References

Abbate, E., & Sagri, M. (1980). Volcanites of Ethiopian and Somali Plateaus and major tectonic lines. *Atti Convegni Lincei*, *47*, 219–227.

Abebe Adhana, T. (2014). The occurrence of a complete continental rift type of volcanic rocks suite along the Yerer–Tullu Wellel Volcano Tectonic Lineament, Central Ethiopia. *Journal of African Earth Sciences*, *99*, 374–385. https://doi.org/10.1016/j.jafrearsci.2014.02.008

Abers, G. A., Fischer, K. M., Hirth, G., Wiens, D. A., Plank, T., Holtzman, B. K., et al. (2014). Reconciling mantle attenuation-temperature relationships from seismology, petrology, and laboratory measurements. *Geochemistry, Geophysics, Geosystems*, *15*(9), 3521–3542. https://doi.org/10.1002/2014GC005444

Abers, G. A., & Hacker, B. R. (2016). A MATLAB toolbox and Excel workbook for calculating the densities, seismic wave speeds, and major element composition of minerals and rocks at pressure and temperature. *Geochemistry, Geophysics, Geosystems*, *17*(2), 616–624. https://doi.org/10.1002/2015GC006171

Abossie, A., Fisseha, S., & Abebe, B. (2023). Crustal resistivity structures beneath the western flank across the Central Main Ethiopian Rift: Its implications for partial melt and pathways. *Journal of Volcanology and Geothermal Research*, *441*, 107888. https://doi.org/10.1016/j.jvolgeores.2023.107888

Accardo, N. J. (2018). *Constraints on the structure and evolution of the Malawi Rift from active-and passive-source seismic imaging* (PhD Thesis). Columbia Univesity. Retrieved from https://www.proquest.com/dissertations-theses/constraints-on-structure-evolution-malawi-rift/docview/2021974950/se-2?accountid=14522

Accardo, N. J., Shillington, D. J., Gaherty, J. B., Scholz, C. A., Nyblade, A. A., Chindandali, P. R. N., et al. (2018). Constraints on rift basin structure and border fault growth in the northern Malawi Rift from 3-D seismic refraction imaging. *Journal of Geophysical Research: Solid Earth*, *123*(11). https://doi.org/10.1029/2018JB016504

Adenis, A., Debayle, E., & Ricard, Y. (2017). Attenuation tomography of the upper mantle. *Geophysical Research Letters*, *44*(15), 7715–7724. https://doi.org/10.1002/2017GL073751

Ahmed, A., Doubre, C., Leroy, S., Keir, D., Pagli, C., Hammond, J. O. S., et al. (2022). Across and along-strike crustal structure variations of the western Afar margin and adjacent plateau: Insights from receiver functions analysis. *Journal of African Earth Sciences*, *192*, 104570. https://doi.org/10.1016/j.jafrearsci.2022.104570

21699356, 2025, 2, Downloaded from https://agupubs.onlinelibrary.wiley.com/doi/10.1029/2024JB030417 by University Of California Santa Barbara, Wiley Online Library on [14/02/2025]. See the Terms and Conditions (https://onlinelibrary.wiley.com/terms-and-conditions) on Wiley Online Library for rules of use; OA articles are governed by the applicable Creative Commons License

Albuquerque Seismological Laboratory/USGS. (1988). Global Seismograph Network (GSN - IRIS/USGS) [Dataset]. *International Federation of Digital Seismograph Networks*. https://doi.org/10.7914/SN/IU

Alemayehu, S., Aoudia, A., Ayele, A., Pachhai, S., Thapa, H. R., Ebinger, C. J., et al. (2023). Structure of the crust-uppermost mantle beneath the Ethiopian volcanic province using ambient seismic noise and teleseismic P wave coda autocorrelation. *Tectonophysics*, *869*, 230092. https://doi.org/10.1016/j.tecto.2023.230092

Allen, R. M., Nolet, G., Morgan, W. J., Vogfjörd, K., Bergsson, B. H., Erlendsson, P., et al. (1999). The thin hot plume beneath Iceland. *Geophysical Journal International*, *137*(1), 51–63. https://doi.org/10.1046/j.1365-246x.1999.00753.x

Armitage, J. J., Ferguson, D. J., Goes, S., Hammond, J. O. S., Calais, E., Rychert, C. A., & Harmon, N. (2015). Upper mantle temperature and the onset of extension and break-up in Afar, Africa. *Earth and Planetary Science Letters*, *418*, 78–90. https://doi.org/10.1016/j.epsl.2015.02.039

Asefa, J., & Ayele, A. (2021). Seismicity of the East African Rift System for the period 2013 to 2016. *Journal of African Earth Sciences*, *183*, 104315. https://doi.org/10.1016/j.jafrearsci.2021.104315

Asplet, J., Wookey, J., Kendall, M., Chapman, M., & Das, R. (2024). Shear-wave attenuation anisotropy: A new constraint on mantle melt near the Main Ethiopian Rift. *Seismica*, *3*(1). https://doi.org/10.26443/seismica.v3i1.1098

Austin, N. J., & Evans, B. (2007). Paleowattmeters: A scaling relation for dynamically recrystallized grain size. *Geology*, *35*(4), 343–346. https://doi.org/10.1130/g23244a.1

Bastow, I. D., & Keir, D. (2011). The protracted development of the continent-ocean transition in Afar. *Nature*, *4*(4), 248–250. https://doi.org/10.1038/ngeo1095

Bastow, I. D., Keir, D., & Daly, E. (2011). The Ethiopia Afar Geoscientific Lithospheric Experiment (EAGLE): Probing the transition from continental rifting to incipient seafloor spreading [Dataset]. In L. Beccaluva, G. Bianchini, & M. Wilson (Eds.), *Volcanism and evolution of the African lithosphere*. Geological Society of America. https://doi.org/10.1130/2011.2478(04)

Bastow, I. D., Nyblade, A., Stuart, G., Rooney, T., & Benoit, M. (2008). Upper mantle seismic structure beneath the Ethiopian hot spot: Rifting at the edge of the African low-velocity anomaly. *Geochemistry, Geophysics, Geosystems*, *9*(12). https://doi.org/10.1029/2008GC002107

Bastow, I. D., Pilidou, S., Kendall, J.-M., & Stuart, G. W. (2010). Melt-induced seismic anisotropy and magma assisted rifting in Ethiopia: Evidence from surface waves. *Geochemistry, Geophysics, Geosystems*, *11*(6). https://doi.org/10.1029/2010GC003036

Bastow, I. D., Stuart, G. W., Kendall, J. M., & Ebinger, C. J. (2005). Upper-mantle seismic structure in a region of incipient continental breakup: Northern Ethiopian rift. *Geophysical Journal of the Royal Astronomical Society*, *162*(2), 479–493. https://doi.org/10.1111/j.1365-246x.2005.02666.x

Benoit, M. H., Nyblade, A. A., Owens, T. J., & Stuart, G. (2006). Mantle transition zone structure and upper mantle S velocity variations beneath Ethiopia: Evidence for a broad, deep-seated thermal anomaly. *Geochemistry, Geophysics, Geosystems*, *7*(11). https://doi.org/10.1029/2006GC001398

Benoit, M. H., Nyblade, A. A., & Pasyanos, M. E. (2006). Crustal thinning between the Ethiopian and East African plateaus from modeling Rayleigh wave dispersion. *Geophysical Research Letters*, *33*(13). https://doi.org/10.1029/2006gl025687

Berckhemer, H., Baier, B., Bartelsen, H., Behle, A., Burkhardt, H., Gebrande, H., et al. (1975). Deep seismic soundings in the Afar region and on the highland of Ethiopia. *Afar Depression of Ethiopia*, *1*, 89–107.

Bezada, M. J., Byrnes, J., & Eilon, Z. (2019). On the robustness of attenuation measurements on teleseismic P waves: Insights from micro-array analysis of the 2017 North Korean nuclear test. *Geophysical Journal International*, *218*(1), 573–585. https://doi.org/10.1093/gji/ggz169

Bialas, R. W., Buck, W. R., & Qin, R. (2010). How much magma is required to rift a continent? *Earth and Planetary Science Letters*, *292*(1–2), 68–78. https://doi.org/10.1016/j.epsl.2010.01.021

Bilham, R., Bendick, R., Larson, K., Mohr, P., Braun, J., Tesfaye, S., & Asfaw, L. (1999). Secular and tidal strain across the Main Ethiopian Rift. *Geophysical Research Letters*, *26*(18), 2789–2792. https://doi.org/10.1029/1998GL005315

Birhanu, Y., Bendick, R., Fisseha, S., Lewi, E., Floyd, M., King, R., & Reilinger, R. (2016). GPS constraints on broad scale extension in the Ethiopian Highlands and Main Ethiopian Rift. *Geophysical Research Letters*, *43*(13), 6844–6851. https://doi.org/10.1002/2016gl069890

Boyce, A., Bastow, I. D., Cottaar, S., Kounoudis, R., Guilloud De Courbeville, J., Caunt, E., & Desai, S. (2021). AFRP20: New *P* -wavespeed model for the African mantle reveals two whole-mantle plumes below East Africa and neoproterozoic modification of the Tanzania craton. *Geochemistry, Geophysics, Geosystems*, *22*(3). https://doi.org/10.1029/2020GC009302

Boyce, A., Kounoudis, R., Bastow, I. D., Cottaar, S., Ebinger, C. J., & Ogden, C. S. (2023). Mantle wavespeed and discontinuity structure below East Africa: Implications for cenozoic hotspot tectonism and the development of the Turkana depression. *Geochemistry, Geophysics, Geosystems*, *24*(8), e2022GC010775. https://doi.org/10.1029/2022GC010775

Brunsvik, B. R., Eilon, Z. C., & Lynner, C. (2021). Mantle structure and flow across the continent-ocean transition of the eastern north American margin: Anisotropic *S* -wave tomography. *Geochemistry, Geophysics, Geosystems*, *22*(12). https://doi.org/10.1029/2021GC010084

Buck, W. R. (1991). Modes of continental lithospheric extension. *Journal of Geophysical Research*, *96*(B12), 20161–20178. https://doi.org/10.1029/91JB01485

Buck, W. R. (2004). Consequences of asthenospheric variability on continental rifting. In G. D. Karner, B. Taylor, N. W. Driscoll, & D. L. Kohlstedt (Eds.), *Rheology and deformation of the lithosphere at continental margins* (pp. 1–30). Columbia University Press. https://doi.org/10.7312/karn12738-002

Buck, W. R. (2006). The role of magma in the development of the Afro-Arabian Rift System. *Geological Society, London, Special Publications*, *259*(1), 43–54. https://doi.org/10.1144/GSL.SP.2006.259.01.05

Budiansky, B., & O'Connell, R. (1980). Bulk dissipation in heterogeneous media. *Solid Earth Geophysics and Geotechnology*, *42*, 1–10.

Cafferky, S., & Schmandt, B. (2015). Teleseismic P wave spectra from US array and implications for upper mantle attenuation and scattering. *Geochemistry, Geophysics, Geosystems*, *16*(10), 3343–3361. https://doi.org/10.1002/2015gc005993/pdf

Chambers, E. L., Harmon, N., Keir, D., & Rychert, C. A. (2019). Using ambient noise to image the Northern East African Rift. *Geochemistry, Geophysics, Geosystems*, *20*(4), 2091–2109. https://doi.org/10.1029/2018GC008129

Chambers, E. L., Harmon, N., Rychert, C. A., Gallacher, R. J., & Keir, D. (2022). Imaging the seismic velocity structure of the crust and upper mantle in the northern East African Rift using Rayleigh wave tomography. *Geophysical Journal International*, *230*(3), 2036–2055. https://doi.org/10.1093/gji/ggac156

Chambers, E. L., Harmon, N., Rychert, C. A., & Keir, D. (2021). Variations in melt emplacement beneath the northern East African Rift from radial anisotropy. *Earth and Planetary Science Letters*, *573*, 117150. https://doi.org/10.1016/j.epsl.2021.117150

Chang, S., Kendall, E., Davaille, A., & Ferreira, A. M. G. (2020). The evolution of mantle plumes in East Africa. *Journal of Geophysical Research: Solid Earth*, *125*(12). https://doi.org/10.1029/2020JB019929

Chiasera, B., Rooney, T. O., Girard, G., Yirgu, G., Grosfils, E., Ayalew, D., et al. (2018). Magmatically assisted off-rift extension—The case for broadly distributed strain accommodation. *Geosphere*, *14*(4), 1544–1563. https://doi.org/10.1130/GES01615.1

21699356, 2025, 2, Downloaded from https://agupubs.onlinelibrary.wiley.com/doi/10.1029/2024JB030417 by University Of California Santa Barbara, Wiley Online Library on [14/02/2025]. See the Terms and Conditions (https://onlinelibrary.wiley.com/terms-and-conditions) on Wiley Online Library for rules of use; OA articles are governed by the applicable Creative Commons License

Civiero, C., Goes, S., Hammond, J. O. S., Fishwick, S., Ahmed, A., Ayele, A., et al. (2016). Small-scale thermal upwellings under the northern East African Rift from *S* travel time tomography: Small Upwellings Below East Africa. *Journal of Geophysical Research: Solid Earth*, *121*(10), 7395–7408. https://doi.org/10.1002/2016JB013070

Civiero, C., Hammond, J. O. S., Goes, S., Fishwick, S., Ahmed, A., Ayele, A., et al. (2015). Multiple mantle upwellings in the transition zone beneath the northern East-African Rift system from relative P-wave travel-time tomography. *Geochemistry, Geophysics, Geosystems*, *16*(9), 2949–2968. https://doi.org/10.1002/2015GC005948

Civiero, C., Lebedev, S., & Celli, N. L. (2022). A complex mantle plume head below East Africa-Arabia shaped by the lithosphere-asthenosphere boundary topography. *Geochemistry, Geophysics, Geosystems*, *23*(11). https://doi.org/10.1029/2022GC010610

Cornwell, D., Maguire, P., England, R., & Stuart, G. (2010). Imaging detailed crustal structure and magmatic intrusion across the Ethiopian Rift using a dense linear broadband array. *Geochemistry, Geophysics, Geosystems*, *11*(1). https://doi.org/10.1029/2009gc002637

Corti, G., Maestrelli, D., & Sani, F. (2022). Large-to local-scale control of pre-existing structures on continental rifting: Examples from the main Ethiopian rift, East Africa. *Frontiers in Earth Science*, *10*, 808503. https://doi.org/10.3389/feart.2022.808503

Corti, G., Molin, P., Sembroni, A., Bastow, I. D., & Keir, D. (2018). Control of pre-rift lithospheric structure on the architecture and evolution of continental rifts: Insights from the Main Ethiopian Rift, East Africa. *Tectonics*, *37*(2), 477–496. https://doi.org/10.1002/2017TC004799

Dalton, C. A., Ekström, G., & Dziewonski, A. M. (2009). Global seismological shear velocity and attenuation: A comparison with experimental observations. *Earth and Planetary Science Letters*, *284*(1–2), 65–75. https://doi.org/10.1016/j.epsl.2009.04.009

Dannberg, J., Eilon, Z., Faul, U., Gassmöller, R., Moulik, P., & Myhill, R. (2017). The importance of grain size to mantle dynamics and seismological observations. *Geochemistry, Geophysics, Geosystems*, *18*(8), 3034–3061. https://doi.org/10.1002/2017GC006944

Dasgupta, R., & Hirschmann, M. M. (2010). The deep carbon cycle and melting in Earth's interior. *Earth and Planetary Science Letters*, *298*(1–2), 1–13. https://doi.org/10.1016/j.epsl.2010.06.039

Dasgupta, R., Mallik, A., Tsuno, K., Withers, A. C., Hirth, G., & Hirschmann, M. M. (2013). Carbon-dioxide-rich silicate melt in the Earth's upper mantle. *Nature*, *493*(7431), 211–215. https://doi.org/10.1038/nature11731

Debayle, E., Bodin, T., Durand, S., & Ricard, Y. (2020). Seismic evidence for partial melt below tectonic plates. *Nature*, *586*(7830), 555–559. https://doi.org/10.1038/s41586-020-2809-4

Di Paola, G. M. (1972). The Ethiopian Rift Valley (between 7° 00′ and 8° 40′ lat. north). *Bulletin Volcanologique*, *36*, 517–560. https://doi.org/10.1007/bf02599823

Dixon, J., Clague, D. A., Cousens, B., Monsalve, M. L., & Uhl, J. (2008). Carbonatite and silicate melt metasomatism of the mantle surrounding the Hawaiian plume: Evidence from volatiles, trace elements, and radiogenic isotopes in rejuvenated-stage lavas from Niihau, Hawaii. *Geochemistry, Geophysics, Geosystems*, *9*(9). https://doi.org/10.1029/2008GC002076

Driscoll, N. W., & Karner, G. D. (1998). Lower crustal extension across the Northern Carnarvon basin, Australia: Evidence for an eastward dipping detachment. *Journal of Geophysical Research*, *103*(B3), 4975–4991. https://doi.org/10.1029/97JB03295

Dugda, M. T., Nyblade, A. A., & Julia, J. (2007). Thin lithosphere beneath the Ethiopian plateau revealed by a joint inversion of Rayleigh wave group velocities and receiver functions. *Journal of Geophysical Research*, *112*(B8), B08305. https://doi.org/10.1029/2006JB004918

Dugda, M. T., Nyblade, A. A., Julia, J., Langston, C. A., Ammon, C. J., & Simiyu, S. (2005). Crustal structure in Ethiopia and Kenya from receiver function analysis: Implications for rift development in eastern Africa. *Journal of Geophysical Research*, *110*(B1). https://doi.org/10.1029/2004jb003065

Durek, J. J., & Ekström, G. (1995). Evidence of bulk attenuation in the asthenosphere from recordings of the Bolivia Earthquake. *Geophysical Research Letters*, *22*(16), 2309–2312. https://doi.org/10.1029/95GL01434

Durek, J. J., & Ekström, G. (1996). A radial model of anelasticity consistent with long-period surface-wave attenuation. *Bulletin of the Seismological Society of America*, *86*(1A), 144–158. https://doi.org/10.1785/bssa08601a0144

Dziewonski, A. M., & Anderson, D. L. (1981). Preliminary reference Earth model. *Physics of the Earth and Planetary Interiors*, *25*(4), 297–356. https://doi.org/10.1016/0031-9201(81)90046-7

Ebinger, C. J., & Casey, M. (2001). Continental breakup in magmatic provinces: An Ethiopian example. *Geology*, *29*(6), 527. https://doi.org/10.1130/0091-7613(2001)029<0527:CBIMPA>2.0.CO;2

Ebinger, C. J., & Hayward, N. J. (1996). Soft plates and hot spots: Views from Afar. *Journal of Geophysical Research*, *101*(B10), 21859–21876. https://doi.org/10.1029/96JB02118

Ebinger, C. J., Keir, D., Ayele, A., Calais, E., Wright, T. J., Belachew, M., et al. (2008). Capturing magma intrusion and faulting processes during continental rupture: Seismicity of the Dabbahu (Afar) rift. *Geophysical Journal International*, *174*(3), 1138–1152. https://doi.org/10.1111/j.1365-246X.2008.03877.x

Eilon, Z., Abers, G. A., & Gaherty, J. B. (2016). A joint inversion for shear velocity and anisotropy: The Woodlark Rift, Papua New Guinea. *Geophysical Journal International*, *206*(2), 807–824. https://doi.org/10.1093/gji/ggw177

Eilon, Z., Abers, G. A., Gaherty, J. B., & Jin, G. (2015). Imaging continental breakup using teleseismic body waves: The Woodlark Rift, Papua New Guinea. *Geochemistry, Geophysics, Geosystems*, *16*(8), 2529–2548. https://doi.org/10.1002/2015GC005835

Eilon, Z. C. (2024). Attenuation and velocity tomography of the Northern East African Rift [Dataset]. *Dryad*. https://doi.org/10.5061/dryad.573n5tbj8

Eilon, Z. C., & Abers, G. A. (2017). High seismic attenuation at a mid-ocean ridge reveals the distribution of deep melt. *Science Advances*, *3*(5), e1602829. https://doi.org/10.1126/sciadv.1602829

Emry, E. L., Shen, Y., Nyblade, A. A., Flinders, A., & Bao, X. (2019). Upper mantle Earth structure in Africa from full-wave ambient noise tomography. *Geochemistry, Geophysics, Geosystems*, *20*(1), 120–147. https://doi.org/10.1029/2018GC007804

Eshetu, A., Mammo, T., & Tilmann, F. (2021). Imaging the Ethiopian rift region using transdimensional hierarchical seismic noise tomography. *Pure and Applied Geophysics*, *178*(11), 4367–4388. https://doi.org/10.1007/s00024-021-02880-2

Faul, U. H., Fitz Gerald, J. D., & Jackson, I. (2004). Shear wave attenuation and dispersion in melt-bearing olivine polycrystals: 2. Microstructural interpretation and seismological implications. *Journal of Geophysical Research*, *109*(B6). https://doi.org/10.1029/2003JB002407

Ferguson, D. J., Maclennan, J., Bastow, I. D., Pyle, D. M., Jones, S. M., Keir, D., et al. (2013). Melting during late-stage rifting in Afar is hot and deep. *Nature*, *499*(7456), 70–73. https://doi.org/10.1038/nature12292

Ferrando, S., Frezzotti, M. L., Neumann, E.-R., De Astis, G., Peccerillo, A., Dereje, A., et al. (2008). Composition and thermal structure of the lithosphere beneath the Ethiopian plateau: Evidence from mantle xenoliths in basanites, Injibara, Lake Tana Province. *Mineralogy and Petrology*, *93*(1–2), 47–78. https://doi.org/10.1007/s00710-007-0219-z

Freitas, D., Manthilake, G., Chantel, J., Bouhifd, M. A., & Andrault, D. (2019). Simultaneous measurements of electrical conductivity and seismic wave velocity of partially molten geological materials: Effect of evolving melt texture. *Physics and Chemistry of Minerals*, *46*(6), 535–551. https://doi.org/10.1007/s00269-019-01021-5

21699356, 2025, 2, Downloaded from https://agupubs.onlinelibrary.wiley.com/doi/10.1029/2024JB030417 by University Of California Santa Barbara, Wiley Online Library on [14/02/2025]. See the Terms and Conditions (https://onlinelibrary.wiley.com/terms-and-conditions) on Wiley Online Library for rules of use; OA articles are governed by the applicable Creative Commons License

Gani, N. D. S., Abdelsalam, M. G., Gera, S., & Gani, M. R. (2009). Stratigraphic and structural evolution of the Blue Nile Basin, Northwestern Ethiopian Plateau. *Geological Journal*, *44*(1), 30–56. https://doi.org/10.1002/gj.1127

Gauntlett, M., Stephenson, S. N., Kendall, J.-M., Ogden, C., Hammond, J. O. S., Hudson, T., et al. (2024). The dynamic crust of northern Afar and adjacent rift margins: New evidence from receiver function analysis in Eritrea and Ethiopia. *Geochemistry, Geophysics, Geosystems*, *25*(6), e2023GC011314. https://doi.org/10.1029/2023GC011314

GEOFON Data Centre. (1993). GEOFON seismic network. *GFZ Data Services. Dataset/Seismic Network*. https://doi.org/10.14470/TR560404

Guidarelli, M., Stuart, G., Hammond, J. O. S., Kendall, J. M., Ayele, A., & Belachew, M. (2011). Surface wave tomography across Afar, Ethiopia: Crustal structure at a rift triple-junction zone. *Geophysical Research Letters*, *38*(24). https://doi.org/10.1029/2011GL046840

Halldórsson, S. A., Hilton, D. R., Marshall, E. W., Ranta, E., Ingvason, A., Chakraborty, S., et al. (2022). Evidence from gas-rich ultramafic xenoliths for Superplume-derived recycled volatiles in the East African sub-continental mantle. *Chemical Geology*, *589*, 120682. https://doi.org/10.1016/j.chemgeo.2021.120682

Hammond, J. O. S. (2014). Constraining melt geometries beneath the Afar Depression, Ethiopia from teleseismic receiver functions: The anisotropic H-κ stacking technique. *Geochemistry, Geophysics, Geosystems*, *15*(4), 1316–1332. https://doi.org/10.1002/2013GC005186

Hammond, J. O. S., & Kendall, J.-M. (2016). Constraints on melt distribution from seismology: A case study in Ethiopia. *Geological Society, London, Special Publications*, *420*(1), 127–147. https://doi.org/10.1144/SP420.14

Hammond, J. O. S., Kendall, J.-M., Stuart, G. W., Ebinger, C. J., Bastow, I. D., Keir, D., et al. (2013). Mantle upwelling and initiation of rift segmentation beneath the Afar Depression. *Geology*, *41*(6), 635–638. https://doi.org/10.1130/G33925.1

Hammond, J. O. S., Kendall, J.-M., Stuart, G. W., Keir, D., Ebinger, C., Ayele, A., & Belachew, M. (2011). The nature of the crust beneath the Afar triple junction: Evidence from receiver functions. *Geochemistry, Geophysics, Geosystems*, *12*(12). https://doi.org/10.1029/2011GC003738

Hammond, J. O. S., Kendall, J.-M., Wookey, J., Stuart, G. W., Keir, D., & Ayele, A. (2014). Differentiating flow, melt, or fossil seismic anisotropy beneath Ethiopia. *Geochemistry, Geophysics, Geosystems*, *15*(5), 1878–1894. https://doi.org/10.1002/2013GC005185

Hammond, W. C., & Humphreys, E. D. (2000a). Upper mantle seismic wave attenuation: Effects of realistic partial melt distribution. *Journal of Geophysical Research*, *105*(B5), 10987–10999. https://doi.org/10.1029/2000JB900042

Hammond, W. C., & Humphreys, E. D. (2000b). Upper mantle seismic wave velocity: Effects of realistic partial melt geometries. *Journal of Geophysical Research*, *105*(B5), 10975–10986. https://doi.org/10.1029/2000JB900041

Hansen, S. E., & Nyblade, A. A. (2013). The deep seismic structure of the Ethiopia/Afar hotspot and the African superplume. *Geophysical Journal International*, *194*(1), 118–124. https://doi.org/10.1093/gji/ggt116

Havlin, C., Holtzman, B. K., & Hopper, E. (2021). Inference of thermodynamic state in the asthenosphere from anelastic properties, with applications to North American upper mantle. *Physics of the Earth and Planetary Interiors*, *314*, 106639. https://doi.org/10.1016/j.pepi.2020.106639

Havlin, C., Parmentier, E. M., & Hirth, G. (2013). Dike propagation driven by melt accumulation at the lithosphere–asthenosphere boundary. *Earth and Planetary Science Letters*, *376*, 20–28. https://doi.org/10.1016/j.epsl.2013.06.010

Heinz, D., Jeanloz, R., & O'Connell, R. J. (1982). Bulk attenuation in a polycrystalline Earth. *Journal of Geophysical Research*, *87*(B9), 7772–7778. https://doi.org/10.1029/JB087iB09p07772

Hirschmann, M. M. (2000). Mantle solidus: Experimental constraints and the effects of peridotite composition. *Geochemistry, Geophysics, Geosystems*, *1*(10), 2000GC000070. https://doi.org/10.1029/2000GC000070

Hirschmann, M. M. (2006). Water, melting, and the deep Earth H2O cycle. *Annual Review of Earth and Planetary Sciences*, *34*(1), 629–653. https://doi.org/10.1146/annurev.earth.34.031405.125211

Holtzman, B. K. (2016). Questions on the existence, persistence, and mechanical effects of a very small melt fraction in the asthenosphere. *Geochemistry, Geophysics, Geosystems*, *17*(2), 470–484. https://doi.org/10.1002/2015GC006102

Holtzman, B. K., & Kendall, J. M. (2010). Organized melt, seismic anisotropy, and plate boundary lubrication. *Geochemistry, Geophysics, Geosystems*, *11*(12), Q0AB06. https://doi.org/10.1029/2010GC003296

Hosseini, K., Matthews, K. J., Sigloch, K., Shephard, G. E., Domeier, M., & Tsekhmistrenko, M. (2018). SubMachine: Web-based tools for exploring seismic tomography and other models of Earth's deep interior. *Geochemistry, Geophysics, Geosystems*, *19*(5), 1464–1483. https://doi.org/10.1029/2018GC007431

Hwang, Y. K., Ritsema, J., & Goes, S. (2011). Global variation of body-wave attenuation in the upper mantle from teleseismic P wave and S wave spectra. *Geophysical Research Letters*, *38*(8), L08311. https://doi.org/10.1029/2011gl046812

Institut de physique du globe de Paris (IPGP)École et Observatoire des Sciences de la Terre de Strasbourg (EOST). (1982). GEOSCOPE, French Global Network of broad band seismic stations [Dataset]. Institut de physique du globe de Paris (IPGP), Université de Paris. https://doi.org/10.18715/GEOSCOPE.G

Jackson, I., Gerald, J. D. F., Faul, U. H., & Tan, B. H. (2002). Grain-size-sensitive seismic wave attenuation in polycrystalline olivine. *Journal of Geophysical Research*, *107*(B12). ECV 5-1-ECV 5-16. https://doi.org/10.1029/2001jb001225

Keir, D., Bastow, I. D., Pagli, C., & Chambers, E. L. (2013). The development of extension and magmatism in the Red Sea rift of Afar. *Tectonophysics*, *607*, 98–114. https://doi.org/10.1016/j.tecto.2012.10.015

Keir, D., Bastow, I. D., Whaler, K. A., Daly, E., Cornwell, D. G., & Hautot, S. (2009). Lower crustal earthquakes near the Ethiopian rift induced by magmatic processes. *Geochemistry, Geophysics, Geosystems*, *10*(6). https://doi.org/10.1029/2009GC002382

Keir, D., Doubre, C., & Leroy, S. (2017). Afar margin northern profile [Dataset]. *International Federation of Digital Seismograph Networks*. https://doi.org/10.7914/SN/YQ_2017

Keir, D., & Hammond, J. O. S. (2009). AFAR0911 [Dataset]. *International Federation of Digital Seismograph Networks*. https://doi.org/10.7914/SN/2H_2009

Keir, K., & Ayele (2016). Rift valley volcanism past present and future [Dataset]. *International Federation of Digital Seismograph Networks*. https://doi.org/10.7914/SN/Y6_2016

Kendall, J.-M., Stuart, G. W., Ebinger, C. J., Bastow, I. D., & Keir, D. (2005). Magma-assisted rifting in Ethiopia. *Nature*, *433*(7022), 146–148. https://doi.org/10.1038/nature03161

Kennet, B., & Engdahl, E. R. (1991). Traveltimes for global earthquake location and phase identification. *Geophysics Journal International*, *105*, 429–465.

Keranen, K. (2013). Exploring extensional tectonics beyond the Ethiopian Rift [Dataset]. *International Federation of Digital Seismograph Networks*. https://doi.org/10.7914/SN/YY_2013

Keranen, K., & Klemperer, S. L. (2008). Discontinuous and diachronous evolution of the Main Ethiopian Rift: Implications for development of continental rifts. *Earth and Planetary Science Letters*, *265*(1–2), 96–111. https://doi.org/10.1016/j.epsl.2007.09.038

21699356, 2025, 2, Downloaded from https://agupubs.onlinelibrary.wiley.com/doi/10.1029/2024JB030417 by University Of California Santa Barbara, Wiley Online Library on [14/02/2025]. See the Terms and Conditions (https://onlinelibrary.wiley.com/terms-and-conditions) on Wiley Online Library for rules of use; OA articles are governed by the applicable Creative Commons License

Keranen, K. M., Hariharan, A., Alemayehu, S., & Ayele, A. (2018). Focused rifting and magmatism beneath the Ethiopian plateau: A subparallel zone of competing lithospheric deformation offset from the Main Ethiopian Rift, *2018*, V24A-05. In *Presented at the AGU Fall Meeting Abstracts*.

Keranen, K. M., Klemperer, S. L., Julia, J., Lawrence, J. F., & Nyblade, A. A. (2009). Low lower crustal velocity across Ethiopia: Is the Main Ethiopian Rift a narrow rift in a hot craton? *Geochemistry, Geophysics, Geosystems*, *10*(5). https://doi.org/10.1029/2008gc002293

Kibret, B. A., Ayele, A., & Keir, D. (2022). Modelling S-wave velocity structure beneath the central Main Ethiopian Rift using receiver functions. *Frontiers in Earth Science*, *10*, 773783. https://doi.org/10.3389/feart.2022.773783

Kibret, B. A., Ayele, A., & Keir, D. (2023). Crustal structure of the Ethiopian Northwestern Plateau and central Afar from receiver function analysis. *Frontiers in Earth Science*, *11*, 1170907. https://doi.org/10.3389/feart.2023.1170907

Kieffer, B., Arndt, N., Lapierre, H., Bastien, F., Bosch, D., Pecher, A., et al. (2004). Flood and shield basalts from Ethiopia: Magmas from the African superswell. *Journal of Petrology*, *45*(4), 793–834. https://doi.org/10.1093/petrology/egg112

Kim, S., Nyblade, A. A., Rhie, J., Baag, C.-E., & Kang, T.-S. (2012). Crustal *S* -wave velocity structure of the Main Ethiopian Rift from ambient noise tomography. *Geophysical Journal International*, *191*(2), 865–878. https://doi.org/10.1111/j.1365-246X.2012.05664.x

Kington, J. D., & Goodliffe, A. M. (2008). Plate motions and continental extension at the rifting to spreading transition in Woodlark Basin, Papua New Guinea: Can oceanic plate kinematics be extended into continental rifts? *Tectonophysics*, *458*(1–4), 82–95. https://doi.org/10.1016/j.tecto.2007.11.027

Knappe, E., Bendick, R., Ebinger, C., Birhanu, Y., Lewi, E., Floyd, M., et al. (2020). Accommodation of East African rifting across the Turkana depression. *Journal of Geophysical Research: Solid Earth*, *125*(2). https://doi.org/10.1029/2019JB018469

Kolawole, F., Phillips, T. B., Atekwana, E. A., & Jackson, C. A.-L. (2021). Structural inheritance controls strain distribution during early continental rifting, Rukwa Rift. *Frontiers in Earth Science*, *9*, 707869. https://doi.org/10.3389/feart.2021.707869

Korostelev, F., Weemstra, C., Leroy, S., Boschi, L., Keir, D., Ren, Y., et al. (2015). Magmatism on rift flanks: Insights from ambient noise phase velocity in Afar region. *Geophysical Research Letters*, *42*(7), 2179–2188. https://doi.org/10.1002/2015GL063259

Koulakov, I., Shapiro, N. M., Sens-Schönfelder, C., Luehr, B. G., Gordeev, E. I., Jakovlev, A., et al. (2020). Mantle and crustal sources of magmatic activity of klyuchevskoy and surrounding volcanoes in Kamchatka inferred from earthquake tomography. *Journal of Geophysical Research: Solid Earth*, *125*(10), e2020JB020097. https://doi.org/10.1029/2020JB020097

Kounoudis, R., Bastow, I. D., Ebinger, C. J., Ogden, C. S., Ayele, A., Bendick, R., et al. (2021). Body-wave tomographic imaging of the Turkana depression: Implications for rift development and plume-lithosphere interactions. *Geochemistry, Geophysics, Geosystems*, *22*(8). https://doi.org/10.1029/2021GC009782

Kumar, U., & Legendre, C. P. (2022). Crust-mantle decoupling beneath Afar revealed by Rayleigh-wave tomography. *Scientific Reports*, *12*(1), 17036. https://doi.org/10.1038/s41598-022-20890-5

Lau, H. C. P., Austermann, J., Holtzman, B. K., Havlin, C., Lloyd, A. J., Book, C., & Hopper, E. (2021). Frequency dependent mantle viscoelasticity via the complex viscosity: Cases from Antarctica. *Journal of Geophysical Research: Solid Earth*, *126*(11). https://doi.org/10.1029/2021JB022622

Lau, H. C. P., Holtzman, B. K., & Havlin, C. (2020). Toward a self-consistent characterization of lithospheric plates using full-spectrum viscoelasticity. *AGU Advances*, *1*(4). https://doi.org/10.1029/2020AV000205

Lavayssière, A., Rychert, C., Harmon, N., Keir, D., Hammond, J. O. S., Kendall, J.-M., et al. (2018). Imaging lithospheric discontinuities beneath the northern East African Rift using S-to-P receiver functions. *Geochemistry, Geophysics, Geosystems*, *19*(10), 4048–4062. https://doi.org/10.1029/2018GC007463

Lavier, L. L., & Manatschal, G. (2006). A mechanism to thin the continental lithosphere at magma-poor margins. *Nature*, *440*(7082), 324–328. https://doi.org/10.1038/nature04608

Lawrence, J. F., & Wysession, M. E. (2006). QLM9: A new radial quality factor (Qμ) model for the lower mantle. *Earth and Planetary Science Letters*, *241*(3–4), 962–971. https://doi.org/10.1016/j.epsl.2005.10.030

Leroy, S., Keir, D., & Stuart, G. (2009). Young conjugate margins lab in the Gulf of Aden [Dataset]. *International Federation of Digital Seismograph Networks*. https://doi.org/10.7914/SN/XW_2009

Levèque, J.-J., & RESIF. (2010). Horn of Africa (Ethiopa, Yemen) broad-band experiment (Horn of Africa, RESIF-SISMOB) [Dataset]. *RESIF - Réseau Sismologique et géodésique Français*. https://doi.org/10.15778/RESIF.YR1999

Ma, Z., Mir, R. R., Dalton, C. A., & Godfrey, K. E. (2024). Choosing appropriate regularization parameters by splitting data into training and validation sets—Application in global surface-wave tomography. *Seismological Research Letters*, *95*(5), 3029–3041. https://doi.org/10.1785/0220230032

Mackenzie, G. D., Thybo, H., & Maguire, P. K. H. (2005). Crustal velocity structure across the Main Ethiopian Rift: Results from two-dimensional wide-angle seismic modelling. *Geophysical Journal International*, *162*(3), 994–1006. https://doi.org/10.1111/j.1365-246X.2005.02710.x

Maestrelli, D., Corti, G., Bonini, M., Montanari, D., & Sani, F. (2022). Caldera collapse and tectonics along the Main Ethiopian Rift: Reviewing possible relationships. *Comptes Rendus Geoscience*, *353*(S2), 91–109. https://doi.org/10.5802/crgeos.63

Maguire, P. K. H., Keller, G. R., Klemperer, S. L., Mackenzie, G. D., Keranen, K., Harder, S., et al. (2006). Crustal structure of the northern Main Ethiopian Rift from the EAGLE controlled-source survey; a snapshot of incipient lithospheric break-up. *Geological Society, London, Special Publications*, *259*(1), 269–292. https://doi.org/10.1144/GSL.SP.2006.259.01.21

Makris, J., & Ginzburg, A. (1987). The Afar Depression: Transition between continental rifting and sea-floor spreading. *Tectonophysics*, *141*(1–3), 199–214. https://doi.org/10.1016/0040-1951(87)90186-7

Manatschal, G. (2004). New models for evolution of magma-poor rifted margins based on a review of data and concepts from West Iberia and the Alps. *International Journal of Earth Sciences*, *93*(3), 432–466. https://doi.org/10.1007/s00531-004-0394-7

Mavko, G., & Nur, A. (1975). Melt squirt in the asthenosphere. *Journal of Geophysical Research*, *80*(11), 1444–1448. https://doi.org/10.1029/JB080i011p01444

Mavko, G. M. (1980). Velocity and attenuation in partially molten rocks. *Journal of Geophysical Research*, *85*(B10), 5173–5189. https://doi.org/10.1029/JB085iB10p05173

McCarthy, C., & Takei, Y. (2011). Anelasticity and viscosity of partially molten rock analogue: Toward seismic detection of small quantities of melt. *Geophysical Research Letters*, *38*(18). https://doi.org/10.1029/2011gl048776

Meshesha, D., & Shinjo, R. (2007). Crustal contamination and diversity of magma sources in the northwestern Ethiopian volcanic province. *Journal of Mineralogical and Petrological Sciences*, *102*(5), 272–290. https://doi.org/10.2465/jmps.061129

Muirhead, J. D., Fischer, T. P., Oliva, S. J., Laizer, A., van Wijk, J., Currie, C. A., et al. (2020). Displaced cratonic mantle concentrates deep carbon during continental rifting. *Nature*, *582*(7810), 67–72. https://doi.org/10.1038/s41586-020-2328-3

21699356, 2025, 2, Downloaded from https://agupubs.onlinelibrary.wiley.com/doi/10.1029/2024JB030417 by University Of California Santa Barbara, Wiley Online Library on [14/02/2025]. See the Terms and Conditions (https://onlinelibrary.wiley.com/terms-and-conditions) on Wiley Online Library for rules of use; OA articles are governed by the applicable Creative Commons License

Nyblade, A. (2000). Seismic investigation of deep structure beneath the Ethiopian Plateau and Afar depression [Dataset]. *International Federation of Digital Seismograph Networks*. https://doi.org/10.7914/SN/XI_2000

O'Connell, R. J., & Budiansky, B. (1977). Viscoelastic properties of fluid-saturated cracked solids. *Journal of Geophysical Research*, *82*(36), 5719–5735. https://doi.org/10.1029/JB082i036p05719

Ogden, C. S., Bastow, I. D., Gilligan, A., & Rondenay, S. (2019). A reappraisal of the H–κ stacking technique: Implications for global crustal structure. *Geophysical Journal International*, *219*(3), 1491–1513. https://doi.org/10.1093/gji/ggz364

Oliveira, R., & Bezada, M. (2023). The Yellowstone paradox. In *Presented at the Interior of the Earth, Gordon Research Conference, 2023, Mount Holyoke, South Hadley, MA*.

Pang, G., Abers, G. A., & Van Keken, P. E. (2023). Focusing effects of teleseismic wavefields by the subducting plate beneath Cascadia. *Journal of Geophysical Research: Solid Earth*, *128*(6), e2022JB025486. https://doi.org/10.1029/2022JB025486

Paxman, G. J. G., Lau, H. C. P., Austermann, J., Holtzman, B. K., & Havlin, C. (2023). Inference of the timescale-dependent apparent viscosity structure in the upper mantle beneath Greenland. *AGU Advances*, *4*(2), e2022AV000751. https://doi.org/10.1029/2022AV000751

Penn State University. (2004). AfricaArray [Dataset]. *International Federation of Digital Seismograph Networks*. https://doi.org/10.7914/SN/AF

Petruska, J., & Eilon, Z. (2022). Distributed extension across the Ethiopian Rift and plateau illuminated by joint inversion of surface waves and scattered body waves. *Geochemistry, Geophysics, Geosystems*, *23*(3). https://doi.org/10.1029/2021GC010179

Rooney, T. O. (2020). The Cenozoic magmatism of East Africa: Part V – Magma sources and processes in the East African Rift. *Lithos*, *360–361*, 105296. https://doi.org/10.1016/j.lithos.2019.105296

Rooney, T. O., Herzberg, C., & Bastow, I. D. (2012). Elevated mantle temperature beneath East Africa. *Geology*, *40*(1), 27–30. https://doi.org/10.1130/G32382.1

Russell, J. B., & Dalton, C. A. (2022). Rayleigh wave attenuation and amplification measured at ocean-bottom seismometer arrays using Helmholtz tomography. *Journal of Geophysical Research: Solid Earth*, *127*(10), e2022JB025174. https://doi.org/10.1029/2022JB025174

Rychert, C. A., Hammond, J. O. S., Harmon, N., Michael Kendall, J., Keir, D., Ebinger, C., et al. (2012). Volcanism in the Afar Rift sustained by decompression melting with minimal plume influence. *Nature Geoscience*, *5*(6), 406–409. https://doi.org/10.1038/ngeo1455

Salas Pazmino, C., & Eilon, Z. (2024). *Inference of thermodynamic state of the upper mantle beneath Alaska using teleseismic body-wave velocity and attenuation tomography T54A-05)*. Presented at the AGU Fall Meeting 2024. Retrieved from https://agu.confex.com/agu/agu24/meetingapp.cgi/Paper/1651339

Schilling, J.-G., Kingsley, R. H., Hanan, B. B., & McCully, B. L. (1992). Nd-Sr-Pb isotopic variations along the Gulf of Aden: Evidence for Afar mantle plume-continental lithosphere interaction. *Journal of Geophysical Research*, *97*(B7), 10927–10966. https://doi.org/10.1029/92jb00415

Schmandt, B., & Humphreys, E. (2010). Seismic heterogeneity and small-scale convection in the southern California upper mantle. *Geochemistry, Geophysics, Geosystems*, *11*(5), Q05004. https://doi.org/10.1029/2010gc003042

Schmeling, H. (1985). Numerical models on the influence of partial melt on elastic, anelastic and electric properties of rocks. Part I: Elasticity and anelasticity. *Physics of the Earth and Planetary Interiors*, *41*(1), 34–57. https://doi.org/10.1016/0031-9201(85)90100-1

Shankland, T. J., O'Connell, R. J., & Waff, H. S. (1981). Geophysical constraints on partial melt in the upper mantle. *Reviews of Geophysics*, *19*(3), 394–406. https://doi.org/10.1029/RG019i003p00394

Shinevar, W. J., Golos, E. M., Jagoutz, O., Behn, M. D., & Van Der Hilst, R. D. (2023). Mantle thermochemical variations beneath the continental United States through petrologic interpretation of seismic tomography. *Earth and Planetary Science Letters*, *602*, 117965. https://doi.org/10.1016/j.epsl.2022.117965

Soto Castaneda, R. A., Abers, G. A., Eilon, Z. C., & Christensen, D. H. (2021). Teleseismic attenuation, temperature, and melt of the upper mantle in the Alaska subduction zone. *Journal of Geophysical Research: Solid Earth*, *126*(7). https://doi.org/10.1029/2021JB021653

Stachnik, J. C., Abers, G. A., & Christensen, D. H. (2004). Seismic attenuation and mantle wedge temperatures in the Alaska subduction zone. *Journal of Geophysical Research*, *109*(B10), B10304. https://doi.org/10.1029/2004jb003018

Stamps, D. S., Kreemer, C., Fernandes, R., Rajaonarison, T. A., & Rambolamanana, G. (2021). Redefining East African Rift System kinematics. *Geology*, *49*(2), 150–155. https://doi.org/10.1130/G47985.1

Stamps, D. S., Saria, E., & Kreemer, C. (2018). A geodetic strain rate model for the East African Rift System. *Scientific Reports*, *8*(1), 1–9. https://doi.org/10.1038/s41598-017-19097-w

Stuart, G. W., Bastow, I. D., & Ebinger, C. J. (2006). Crustal structure of the northern Main Ethiopian Rift from receiver function studies. *Geological Society, London, Special Publications*, *259*(1), 253–267. https://doi.org/10.1144/gsl.sp.2006.259.01.20

Takei, Y. (2002). Effect of pore geometry on *V P/V S: From equilibrium geometry to crack*. *Journal of Geophysical Research*, *107*(B2), 2043. https://doi.org/10.1029/2001JB000522

Takei, Y. (2017). Effects of partial melting on seismic velocity and attenuation: A new insight from experiments. *Annual Review of Earth and Planetary Sciences*, *45*(1), 447–470. https://doi.org/10.1146/annurev-earth-063016-015820

Thompson, D. A., Hammond, J. O. S., Kendall, J.-M., Stuart, G. W., Helffrich, G. R., Keir, D., et al. (2015). Hydrous upwelling across the mantle transition zone beneath the Afar Triple Junction. *Geochemistry, Geophysics, Geosystems*, *16*(3), 834–846. https://doi.org/10.1002/2014GC005648

Thomson, D. J. (1982). Spectrum estimation and harmonic analysis. *Proceedings of the IEEE*, *70*(9), 1055–1096. https://doi.org/10.1109/proc.1982.12433

Trestrail, K. R., Rooney, T. O., Girard, G., Svoboda, C., Yirgu, G., Ayalew, D., & Keppelman, J. (2017). Sub-continental lithospheric mantle deformation in the Yerer-Tullu Wellel Volcanotectonic Lineament: A study of peridotite xenoliths. *Chemical Geology*, *455*, 249–263. https://doi.org/10.1016/j.chemgeo.2016.10.013

Tsekhmistrenko, M., Sigloch, K., Hosseini, K., & Barruol, G. (2021). A tree of Indo-African mantle plumes imaged by seismic tomography. *Nature Geoscience*, *14*(8), 612–619. https://doi.org/10.1038/s41561-021-00762-9

University of Bristol. (2007). Afar consortium network (AFAR) [Dataset]. https://www.fdsn.org/networks/detail/ZF_2007/

Vaišnys, J. R. (1968). Propagation of acoustic waves through a system undergoing phase transformations. *Journal of Geophysical Research*, *73*(24), 7675–7683. https://doi.org/10.1029/JB073i024p07675

VanDecar, J. C., & Crosson, R. S. (1990). Determination of teleseismic relative phase arrival times using multi-channel cross-correlation and least squares. *Bulletin of the Seismological Society of America*, *80*(1), 150–169.

Van Herwaarden, D., Thrastarson, S., Hapla, V., Afanasiev, M., Trampert, J., & Fichtner, A. (2023). Full-waveform tomography of the African plate using dynamic mini-batches. *Journal of Geophysical Research: Solid Earth*, *128*(6), e2022JB026023. https://doi.org/10.1029/2022JB026023

Wang, T., Gao, S. S., Yang, Q., & Liu, K. H. (2021). Crustal structure beneath the Ethiopian Plateau and adjacent areas from receiver functions: Implications for partial melting and magmatic underplating. *Tectonophysics*, *809*, 228857. https://doi.org/10.1016/j.tecto.2021.228857

21699356, 2025, 2, Downloaded from https://agupubs.onlinelibrary.wiley.com/doi/10.1029/2024JB030417 by University Of California Santa Barbara, Wiley Online Library on [14/02/2025]. See the Terms and Conditions (https://onlinelibrary.wiley.com/terms-and-conditions) on Wiley Online Library for rules of use; OA articles are governed by the applicable Creative Commons License

Wei, S. S., & Wiens, D. A. (2020). High bulk and shear attenuation due to partial melt in the Tonga-Lau back-arc mantle. *Journal of Geophysical Research: Solid Earth*, *125*(1). https://doi.org/10.1029/2019JB017527

Wolfenden, E., Ebinger, C., Yirgu, G., Deino, A., & Ayalew, D. (2004). Evolution of the northern Main Ethiopian rift: Birth of a triple junction. *Earth and Planetary Science Letters*, *224*(1–2), 213–228. https://doi.org/10.1016/j.epsl.2004.04.022

Yamauchi, H., & Takei, Y. (2016). Polycrystal anelasticity at near-solidus temperatures. *Journal of Geophysical Research: Solid Earth*, *121*(11), 7790–7820. https://doi.org/10.1002/2016JB013316

Yamauchi, H., & Takei, Y. (2024). Effect of melt on polycrystal anelasticity. *Journal of Geophysical Research: Solid Earth*, *129*(4), e2023JB027738. https://doi.org/10.1029/2023JB027738

21699356, 2025, 2, Downloaded from https://agupubs.onlinelibrary.wiley.com/doi/10.1029/2024JB030417 by University Of California Santa Barbara, Wiley Online Library on [14/02/2025]. See the Terms and Conditions (https://onlinelibrary.wiley.com/terms-and-conditions) on Wiley Online Library for rules of use; OA articles are governed by the applicable Creative Commons License